The folding motion of an axisymmetric jet of wormlike-micelles solution

Matthieu Varagnat [a], Trushant Majmudar [a], Will Hartt [b], Gareth H. McKinley [a]

[a] *Department of Mechanical Engineering, Massachusetts Institute of Technology, Cambridge, 02139 MA, USA*

[b] *Corporate Engineering Technologies Lab, The Procter and Gamble Co, West Chester, OH 45069*

Abstract

The problem of buckling and coiling of jets of viscous, Newtonian liquids has received a substantial level of attention over the past two decades, both from experimental and theoretical points of view. Nevertheless, many industrial fluids and consumer products are non-Newtonian, and their rheological properties affect their flow behavior. The present work aims at studying the dynamics of cylindrical jets of a viscoelastic, shear-thinning solution of cetylpyridinium salt (CPyCl). In concentrated solutions, CPyCl surfactant molecules have been shown to assemble in long wormlike micellar structures, which gives the fluid its non-Newtonian properties. Jets of this fluid show novel features compared to their Newtonian counterparts, including a type of motion, in which the jet folds back and forth on itself in a fashion similar to sheets of viscous fluids, instead of coiling around the vertical axis as cylindrical Newtonian jets do. Another novel feature of CPyCl micellar fluid jets is a widening of the jet above the plate reminiscent of the die-swell phenomenon that we call *reverse swell*. We propose physical mechanisms for both folding and reverse swell, and compare theoretical predictions to experimental measurements. In addition, we systematically explore different flow regimes in the parameter space of the height of fall and flow rate and compare regime maps of a CPyCl micellar solution and a Newtonian silicone oil.

Key words: Micellar fluids, Viscoelastic jets, Jetting, Coiling instability, Folding instability, Buckling

1. Introduction

Situations where a continuous stream of material is flowing downward at a moderate velocity onto a plane surface occur in both everyday life and industrial applications. Honey poured on a toast, the filling of a shampoo bottle in an automated line, as well as numerous other examples in the oil, food, and cosmetic industries, are similar problems in which the stability of the streaming jet is a crucial feature. From an industrial point of view, stable jet spreading homogeneously on the support, is almost always preferred. Indeed, jet instabilities can lead to problems such as the entrapment of air bubbles in the folds of a buckled planar jet as described by Pouligny [1] or the stacking and mounding of yielding materials such as pastes or emulsions. There is therefore a strong practical motivation for understanding the emergence of different flow regimes in this situation and the relevant control parameters.

Depending on the fluid properties, and the control parameters such as the flow rate Q and the height of fall H, a jet can exhibit different behaviors or regimes. At low heights of fall, the jet spreads homogeneously on the plate forming a steady stagnation flow, as shown in Fig. 1(a). Cruickshank and Munson [2] have provided an analytical solution for the shape of the jet, driven by a balance between the imposed flow rate, gravitational acceleration, and the viscous resistance to deformation of the fluid. The shape of the jet is controlled by the parameter $\beta = Ha_0\sqrt{g/6Q\nu}$, where a_0 is the nozzle radius, ν is the kinematic viscosity and g is the acceleration of gravity. For $\beta > \pi/2$, the jet starts to thin under the influence of gravity instead of monotonically enlarging while spreading on the plate. For heights of fall large enough so that $\beta \gg \pi/2$, the jet radius reaches a limit a_1 for which the acceleration of gravity is balanced by the viscous resistance, and the balance of the two forces leads to

$$a_1 \sim \sqrt{\frac{3\nu Q}{Hgl_{VG}}} \tag{1}$$

where $l_{VG} = (\nu^2/g)^{1/3}$ is the characteristic length scale over which gravitational and viscous effects balance each other.

As the height of fall is increased, the jet leaves the stagnation flow regime and starts buckling under the compressive viscous stress, as shown in Fig. 1(b). This situation was first described by Taylor [3] and was studied experimentally by Cruickshank and Munson [4] for planar and axisymmetric jets. The theoretical framework developed by Cruickshank [5] and Tchadarov [6] for

the axisymmetric geometry and by Yarin and Entov [7] for the planar case is in good agreement with these experimental results. Cruickshank showed [5] that the axisymmetric jet can buckle according to two modes, azimuthal and non-azimuthal (called coiling and folding respectively, in this article). They derived a critical buckling height for each mode, given by the following geometrical conditions

$$\frac{H}{2a_0} = 7.663 \text{ (coiling)} \tag{2}$$

$$\frac{H}{2a_0} = 4.810 \text{ (folding)} \tag{3}$$

The validity of Eqs. (2) and (3) have been confirmed experimentally by Cruickshank and Munson [4]. They showed that a cylindrical jet of Newtonian fluid transitions from a steady jet to a coiling one (Fig. 1(c)) at a height given by Eq. (2), and that a planar jet starts folding when the condition in Eq. (3) is satisfied. However, it was also observed that these transitions are suppressed at higher Reynolds numbers [4, 5]. Beyond a critical Reynolds number, an axisymmetric or planar jet exhibits stagnation flow for all nozzle-to-plate distances. The Reynolds number is defined here as the ratio of viscous timescale $t_V = a_0^2/\nu$ to convective timescale $t_I = \pi a_0^3/Q$:

$$Re = \frac{t_V}{t_I} = \frac{Q}{\pi \nu a_0} \tag{4}$$

For axisymmetric jets, the critical Reynolds number above which coiling of the jet disappears is given by:

$$Re_{crit} = \frac{Q}{\pi \nu a_0} \;=\; 1.2 \tag{5}$$

For planar jets, the critical Reynolds number above which folding of the jet disappears is given by:

$$Re_{crit} = \frac{Q}{\pi \nu a_{\mathrm{s}}} \;=\; 0.56 \tag{6}$$

where, a_{s} is the slit radius.

Furthermore, in the cylindrical case, they reported that below this limit, for $0.1 < Re < 1$, two transitions were observed as the height of fall was progressively increased; from a stable jet to folding, and from folding to coiling. The first buckling transition happens roughly at the critical height predicted

by Eq. 3, and the height of the folding-coiling transition is approximately given by Eq. 2. These subtle transitions are difficult to observe experimentally for two reasons; the first reason is that the flow rates required to reach this range of Reynolds number are high, and the second reason is that the values of the scaled height $H/2a_0$, where these transitions occur, are very low. Both of these factors create a situation where a jet whose diameter is almost the same as the nozzle diameter, oscillates under high flow rates at very low nozzle-to-plate distances, making it very difficult to distinguish between coiling and folding.

After the onset of buckling, the jet of a viscous Newtonian fluid starts to coil around the vertical axis, as can be seen in Fig. 2(a). In the limit of large heights of fall, Mahadevan and co-workers [8, 9] derived expressions for the coiling radius and frequency by balancing viscous and inertial forces in the coil; the viscous forces arise from the curvature and bending of the jet in that region. Ribe [10] showed that this analysis was a subset of a broader picture, with three distinct regimes, viscous, gravitational and inertial, depending on which forces were dominant. Ribe's simulations for the frequency of coiling as a function of height, at a given flow rate, were in good agreement with experiments by Maleki and coworkers and showed multi-valued frequencies at the transition between gravitational and inertial regimes [11].

Under the assumption that the jet radius is constant in the coil, the frequency, coiling radius, and the final radius of the jet, are connected by the conservation of volume

$$Q = \pi \Omega R a_1^2 \tag{7}$$

Figure 2(b) schematically details all the relevant forces along the jet length. The resisting torque is always due to viscosity. Viscous bending stresses arise because of the velocity gradient between the inner part of the curved jet, where the velocity is smaller, and the outer part where it is maximum. The velocity gradient scales like $U_1 a_1/R^2$, where $U_1 = Q/\pi a_1^2$ is the axial velocity just before the coil. In a fashion similar to beam-bending in solid mechanics, the viscous stress $\eta Q/\pi R^2 a_1$ integrated over the jet cross-section vanishes, but the integrated torque remains non-zero and scales as [9]

$$T_{coil} \sim \frac{\eta Q a_1^2}{R^2} \tag{8}$$

1.1. Viscous regime

At low heights of fall, the whole tail of the jet is bent sideways and the viscous torque caused by the fixed vertical orientation of the nozzle controls the motion of the jet (the first driving force in Fig. 2(b)). This is also a shear-induced torque, with a characteristic curvature $1/H$, that scales like $\eta Q a_1^2/H^2$. The torque balance leads to the scaling laws for the coiling radius R_V and the coiling frequency Ω_V [10] given by:

$$R_V \sim H \tag{9a}$$

$$\Omega_V \sim \frac{Q}{a_0^2 H} \tag{9b}$$

In this regime, the jet motion is controlled by external parameters such as the height of fall and imposed flow rate, whereas in the other two regimes the fluid jet selects its own dynamics through a balance of forces involving intrinsic fluid properties as well as external parameters.

1.2. Gravitational regime

At larger heights of fall, only the lowest part of the tail is bent, on a length scale of the radius of the coil (R). The weight of the fluid in this part is of the order of $\rho g R a_1^2$, the lever arm is of the order R, and hence the buckling torque is $\rho g R^2 a_1^2$. Using the scaling in Eq. (1) for a_1, the torque balance gives the following scaling laws for the coiling radius R_G and the frequency Ω_G [10]:

$$R_G \sim \left(\frac{\nu Q}{g}\right)^{\frac{1}{4}} \tag{10a}$$

$$\Omega_G \sim H^2 \left(\frac{g^5}{\nu^5 Q}\right)^{\frac{1}{4}} \tag{10b}$$

The transition from viscous to gravitational regime happens [10] for $\Omega_G \simeq 2\Omega_V$, or $H_{VG} \simeq (Q\nu/g)^{5/12} a_0^{-2/3}$. Note that if this height H_{VG} is lower than the buckling height $H_{\mathrm{buckling}} = 7.663 \times 2a_0$, then coiling simply starts in gravitational mode. Indeed, for typical experimental values of $\nu = 200$ cm$^2/s$, $a_0 = 1.25$ mm, and $Q = 3$ mL/min, $H_{\mathrm{VG}} \simeq 0.5$ cm, while $H_{\mathrm{Buckling}} \simeq 1.9$ cm. Note also that a simpler force balance between gravitational and viscous forces given by $\beta \approx 1$, leads to the qualitatively similar result of $H \simeq (Q\nu/g)^{1/2} a_0^{-1}$.

1.3. Inertial regime

When the rotational inertia in the coil becomes important, it can drive the coiling as well. The inertial force in a rotational reference frame scales per unit volume as $\rho\Omega^2 R$, so the torque scales as $\rho\Omega^2 R^3 a_1^2$. The torque balance together with Eqs. (1) and (7) lead to the following scaling laws for the coiling radius R_I and frequency Ω_I [9]:

$$R_I \sim \nu g \left(\frac{Q}{H^4}\right)^{\frac{1}{3}} \tag{11a}$$

$$\Omega_I \sim \frac{1}{\nu^2}\left(\frac{g^5 H^{10}}{Q}\right)^{\frac{1}{3}} \tag{11b}$$

This regime becomes the most stable one when $\Omega_I > 2\Omega_G$ [10], i.e. for $H_{\mathrm{GI}} \simeq (Q\nu^9/g^5)^{1/16}$. For the values used above, this represents a height of approximately $H = 11.0$ cm. Note that for $\Omega_G < \Omega_I < 2\Omega_G$, the system is multivalued, with the solution oscillating between the two possible frequencies. In all of the above analyses the relevant surface tension parameter comparing the capillary thinning process to gravity is much smaller than unity $\sigma/\rho g a_0^2 << 1$, where σ is the surface tension of the fluid. Cruickshank and Munson have reported experimental data for a surface tension parameter slightly larger than one [4], but never to a point where the destabilizing action of capillary forces breaks the jet into droplets.

So far, the research on jets impacting a plate has mostly focused on Newtonian fluids, for example with viscous fluids such as silicone oil. Nevertheless, real-life fluids are almost always more complex: pastes, gels, and surfactants are ubiquitous in the healthcare, cosmetic, and food industries. Rheologically complex fluids are used in many aspects of everyday life; from ketchup and mayonnaise to foaming detergents, skin creams, and hair conditioners. Beyond the industrial interest toward extending the field of study to non-Newtonian fluids, the motivation for this work is to connect the rheology of the fluid to its jetting properties. We focus on jets of wormlike micellar solutions of cetylpyridinium chloride (CPyCl). Wormlike micellar fluids are non-Newtonian fluids that have recently attracted a lot of attention for their strong, tailorable viscoelastic and shear-thinning properties, their ease of use, and the possibility they offer as model fluids for surfactant-based consumer products [12].

Wormlike micellar fluids are concentrated aqueous solutions of one or more ionic surfactants, as well as a counter-ion salt. At very low surfactant

concentration, the solution is homogeneous, but when the concentration increases above a critical threshold, denoted the critical micellar concentration or CMC, the surfactant molecules spontaneously assemble in spherical structures. In these spherical micelles the surfactants orient their organic tails towards the center and bear their ionic heads outside, satisfying both tail segregation and ionic repulsion. Adding a large enough counter-ion reduces the curvature of the optimal shape, by screening the ionic interactions. The change of optimal curvature leads, for some combinations of surfactants and counter-ions, to changes in the shape of the assembly [13]. In some parts of their phase diagrams [14], some carefully chosen systems exhibit long linear structures, called wormlike micelles. The formation of wormlike micellar structure is schematically represented in Fig. 3. In studies of extensional flow of these fluids, Yesilata and co-workers [15] have used solutions of erucyl bis(2-hydroxyethyl) methyl ammonium chloride (EHAC), and Rothstein [16] used cetyltrimethylammonium bromide (CTAB). Rehage and Hoffmann [12], as well as Berret and co-workers [17] have used a solution of CetylPyridinium Chloride (CPyCl) and a salicylic salt (NaSal) in brine and we employ this well characterized system in the present study.

Wormlike structures at high enough concentrations in surfactant and salt are long enough to entangle, therefore giving pronounced viscoelastic properties to the solution. Stress relaxation with wormlike micelles can operate via two processes: the first one is reptation, similar to the stress relaxation process of polymers described by de Gennes [18], and the second one is a breakup-recombination process that is unique to these polymer systems. The characteristic timescales for stress relaxation and breakup-recombination processes are λ_r and λ_b, respectively, and Cates showed that, for $\lambda_b \ll \lambda_r$, the linear viscoelastic properties are well described by a single-relaxation-time Maxwell model with a characteristic timescale λ given by [19]:

$$\lambda = (\lambda_r \lambda_b)^{\frac{1}{2}} \tag{12}$$

In steady shear flow, wormlike micellar solutions are strongly nonlinear fluids, with a characteristic shear rate $1/\lambda$ and a zero-shear-rate viscosity η_0 that is strongly dependent on the salt concentration. For shear rates above $1/\lambda$, it is found that the shear stress exhibits a plateau and remains almost constant at a critical stress of the order of $\lambda\eta_0$. In addition, both λ and η_0 are observed to be strongly temperature dependent, with an Arrhenius-type dependence with a very large activation energy. The strong variations

of rheological properties with temperature come from two effects acting in the same direction. The first is a polymer-like behavior in which reptation, a thermally activated process, occurs more rapidly at higher temperature. The second is specific to supramolecular structures: the breakup rate increases with temperature, which is not only a stress relaxation process on its own, but also tends to shorten the average length of wormlike micelles, thus resulting in a shorter path-length for reptation to occur.

Extensional rheological studies of wormlike micellar solutions conducted using capillary breakup experiments (CaBER) ([15], [20]) have shown a significant extension strengthening of the fluid, likely due to the alignment of the wormlike micelles in the extensional flow [16], quite like what happens for dilute polymer solutions. For example, in the case of CPyCl micellar solutions, Bhardwaj and co-workers have shown [20] that the fluid first undergoes an initial phase of Newtonian visco-capillary thinning [15]. As the liquid bridge thins, the extension rate ($\dot{\epsilon}$) increases, until the local Weissenberg number $Wi_{\rm mid} = \lambda\dot{\epsilon} = 0.5$. At that point the wormlike micelles are stretched too rapidly to relax, which leads to extension thickening, with elastic stress buildup resisting the breakup of the thin filament. In contrast to polymer solutions however, when the local tensile stresses become too large for the micelles to resist, *en masse* rupture of the entangled chains results in filament breakup [16]. In addition, thin liquid bridges and jets have a large area-to-surface ratio, and therefore solvent evaporation can tend to cool the fluid and increase the surfactant concentration, both effects increase the viscosity and lower the thinning rate.

Jets of CPyCl wormlike micellar solution falling on a plate show two novel features. The shape of the jet is different from its Newtonian counterpart, with a widening of the jet immediately above the plate, as we have shown in Fig. 4(a). This feature is reminiscent of the well studied die-swell phenomenon [21], in which jets of non-Newtonian fluids swell at the exit of a nozzle, and we refer to it as *reverse swell*. The first goal of this paper is to understand this novel phenomenon and to predict the amount of swell measured experimentally. The second feature observed in the viscoelastic CPyCl micellar jets is a novel type of dynamic behavior, in which the buckled cylindrical jet remains in a vertical plane and folds back and forth on itself, as shown in Fig. 4(b). For Newtonian fluids the folding motion is observed only for planar jets and never for cylindrical jets. This new type of motion dominates in most experimental cases, but for some values of the experimental parameters, jets of CPyCl micellar solutions can coil instead (see Fig. 4(c)).

The second goal of this paper is to map these different types of instabilities onto a suitable non-dimensional parameter space, and describe a mechanism for this viscoelastic folding. We then derive scaling laws for the amplitude and frequency of folding based on the proposed mechanism, and compare them to the experimental data.

This paper is divided in two sections, theoretical and experimental. We first begin by defining a suitable non-dimensionalization scheme, that allows us to compare CPyCl solutions at different concentrations and contrast the response with other fluids. We then propose a mechanism for the reverse swell phenomenon and the folding behavior of CPyCl jets. We also derive appropriate scaling laws for the amplitudes and frequencies of folding states. Then, we describe the details of the experiments, and compare theoretical predictions to experimental data.

2. Theoretical analysis

2.1. Dimensional analysis

The forces in balance along the flow in the jet are (i) gravity that tends to accelerate and stretch the jet, and (ii) viscosity that resists the process, provided that the height of fall is large enough so that $\beta \gg \pi/2$. This competition can be characterized by a time scale $t_{\mathrm{VG}} = (\nu_0/g^2)^{\frac{1}{3}}$ and a length scale $l_{\mathrm{VG}} = (\nu_0^2/g)^{\frac{1}{3}}$, where ν_0 is the zero-shear-rate kinematic viscosity. These scalings will typically be relevant as long as strain-hardening does not occur; a condition true in most cases, which will be discussed below. For length and time scales larger than these estimates, the jet thins by an amount determined by the balance of the two forces. Therefore, it is reasonable to non-dimensionalize the experimental parameters with these scales to obtain dimensionless heights and flow rates:

$$H^* = \frac{H}{l_{\mathrm{VG}}} = H\left(\frac{g}{\nu_0^2}\right)^{\frac{1}{3}} \tag{13}$$

$$Q^* = \frac{Q\ t_{\mathrm{VG}}}{l_{\mathrm{VG}}^3} = Q\left(\frac{g}{\nu_0^5}\right)^{\frac{1}{3}} \tag{14}$$

At lower heights of fall the relevant scaling for the height is the aspect ratio that is used in Eqs. (2) and (3):

$$\epsilon = \frac{H}{2a_0} \tag{15}$$

This aspect ratio will also be used as a dimensionless height.

The ratio of the elastic relaxation timescale λ to t_{VG} gives rise to an elasto-gravitational number. Non-Newtonian effects arise in the jet when the stretch rate, driven by gravity and resisted by viscosity, becomes larger than the relaxation rate of the wormlike micelles. Therefore, the elasto-gravitational number characterizes the magnitude of these effects

$$E_g = \frac{\lambda}{t_{\mathrm{VG}}} = \lambda \left(\frac{g^2}{\nu_0}\right)^{\frac{1}{3}} \tag{16}$$

In a similar fashion, the radius of the jet at points along its stream ($i = 0, 1, 2$) (Fig. 1 and Fig. 4) can be scaled by the same length scale

$$a_i^* = \frac{a_i}{l_{\mathrm{VG}}} = a_i \left(\frac{g}{\nu_0^2}\right)^{\frac{1}{3}} \tag{17}$$

In the folding regime, the dimensionless measured quantities that we report (i.e. the frequency f and the amplitude L) are scaled in the same fashion:

$$f^* = f\ t_{\mathrm{VG}} = f \left(\frac{\nu_0}{g^2}\right)^{\frac{1}{3}} \tag{18}$$

$$L^* = \frac{L}{l_{\mathrm{VG}}} = L \left(\frac{g}{\nu_0^2}\right)^{\frac{1}{3}} \tag{19}$$

The Reynolds number defined in Eq. (4) can also be rewritten using these expressions as:

$$Re = \frac{Q}{a_0 \nu} = \frac{Q^*}{a_0^*} \tag{20}$$

2.2. Reverse swell

The reverse swell (Fig. 4(a)) is a very peculiar feature of jets of wormlike-micellar fluids, in which the jet widens two to three times its initial radius near the plate, as compared to the thinnest part of the tail. For Newtonian fluids, the jet constantly thins, down to the coil region, beyond which the radius becomes constant. In the case of CPyCl micellar jets, this reverse

swell effect arises from the non-Newtonian viscoelastic character of the fluid. As the fluid accelerates under the effect of gravity, the fluid elements stretch, the wormlike micelles become aligned and store elastic energy. When the local stretching rate becomes weaker, because of the deceleration imposed by the presence of the plate, the stretched molecules recoil, which leads to the observed lateral dilation. A noticeable reverse swell is therefore possible for a Weissenberg number $Wi = \lambda(U_1 - U_0)/H = E_g(H^* - Q^*/a_0^{*2})$ greater than approximately unity. Note that this condition requires $H^* \geq Q^*/a_0^{*2}$, which means that the fluid particles must be accelerated during the fall. For practical purposes (in order to get a measurable reverse swell), a more realistic condition is $H^* \gg Q^*/a_0^{*2}$, which simplifies the condition for reverse swell to

$$Wi = E_g H^* \gg 1 \tag{21}$$

For example, the jet shown in Fig. 4(a) is characterized by a large value of $Wi = 11.3$ and exhibits significant reverse swell. The reverse swell is strongly reminiscent of the die-swell phenomenon, and a derivation similar to that given by Tanner [21] can be used to predict the amount of swelling. The assumption is that no external force acts on the fluid element over the length scale of recoil h, thus we neglect gravity on the scale of $h \ll l_{\mathrm{VG}}$, as well as the reaction of the bottom plate. If N_1 is the first normal stress difference in the fluid just before the swell, P the hydrostatic pressure in the jet, I the identity matrix, and $\alpha = a_2/a_1$ is the swell ratio, the force balance can be written as

$$-PI + \begin{pmatrix} 3G & 0 & 0 \\ 0 & 3G & 0 \\ 0 & 0 & 3G + N_1 \end{pmatrix} \begin{pmatrix} \alpha^2 & 0 & 0 \\ 0 & \alpha^2 & 0 \\ 0 & 0 & \frac{1}{\alpha}^4 \end{pmatrix} = 0$$

This corresponds to three equations with four unknowns. Eliminating P among these equations leads to

$$\alpha = \left(1 + \frac{N_1}{3G}\right)^{\frac{1}{6}} \tag{22}$$

To proceed further, viscoelastic material elements will be considered as purely elastic during the stretch process in the tail of the jet. This does not imply that the elastic component of the total tensile stress in the jet is more important than the viscous part, which would not be true, but only that the

elastic part does not relax during the time of fall, which is legitimate for moderate residence time in the jet and $Wi \gg 1$. We can therefore estimate N_1 from the tensile stresses expected from rubber elasticity theory, given by

$$N_1 = 3G\left(\left(\frac{a_0}{a_1}\right)^4 - \left(\frac{a_1}{a_0}\right)^2\right) \tag{23}$$

We have already assumed that $a_1 \ll a_0$ (significant thinning), therefore a first order approximation of Eq. (23) combined with Eq. (22) gives a swell ratio of

$$\alpha = \left(\frac{a_0}{a_1}\right)^{\frac{2}{3}} \tag{24}$$

In dimensionless form, and using the value for a_1 given by Eq. (1), one finds that the swell ratio α should vary as

$$\alpha = \frac{a_2}{a_1} \sim \left(a_0^{*2}\frac{H^*}{Q^*}\right)^{\frac{1}{3}} \tag{25}$$

Equation (1), which has the form $a_1 \sim (Q/H)^{1/2}(\nu/g^2)^{1/6}$ when omitting the multiplicative constant, can be rewritten in dimensionless terms as

$$a_1^* \sim \sqrt{\frac{Q^*}{H^*}} \tag{26}$$

Combining Eqs. (25) and (26) leads to the following scaling for the final radius:

$$a_2^* \sim \left(a_0^{*\,2}\sqrt{\frac{Q^*}{H^*}}\right)^{\frac{1}{3}} \tag{27}$$

Or in dimensional terms, this becomes

$$a_2 \sim \left(a_0^2\sqrt{\frac{Q}{H}}\right)^{\frac{1}{3}}\left(\frac{\nu_0}{g^2}\right)^{1/18} \tag{28}$$

In addition, the reverse swell process takes place over a vertical length h, determined by the balance between the characteristic speed of the downward flow in the swollen region, which can be averaged to $Q/\pi a_1 a_2$, and the upward

propagation of viscous effects, ν/h. Using Eq. (27), this leads to the following dimensionless expression for h

$$h^* = \frac{h}{l_{\mathrm{VG}}} \sim \left(\frac{a_0^{*4}}{H^{*2} Q^*} \right)^{1/3} \tag{29}$$

This can be written in dimensional terms as

$$h \sim \left(\frac{a_0^4}{H^2 Q} \right)^{1/3} \left(\frac{\nu_0^7}{g^2} \right)^{1/9} \tag{30}$$

Everything else being equal, the height h over which the swell occurs scales as $\nu_0^{7/9}$. This means that viscoelastic fluids with low viscosities will display a sharp reverse swell, whereas for very viscous viscoelastic fluids it may be gradual and hard to discern. Another way to say the same thing is to derive the slope in the swell region, $s = (a_2 - a_1)/h$, using Eqs. (28) and (30). In the limit of $a_2 \gg a_1$ (a rather strong approximation) we obtain

$$s = (a_2 - a_1)/h \sim \frac{(HQ)^{1/2} g^{1/9}}{a_0^{2/3} \nu_0^{13/18}} \tag{31}$$

Equation (31) is of limited validity because the assumption $a_2 \gg a_1$ is not true in most cases, however, it underlines that experimentally noticeable reverse swell requires a fluid with a viscosity as low as possible. Since elasticity is important (from the condition (21)), strongly elastic fluids such as wormlike micellar solutions are ideally suited for observing reverse swell, as opposed to very viscous viscoelastic fluids such as Boger fluids or weakly elastic fluids such as commercial shampoos. Larger values of h also mean that an increased time in the swell is available for the macromolecules to relax, which may invalidate the purely elastic recovery assumption used to derive Eq. (24). As a result, it is not possible at the present time to be certain whether very viscous elastic fluids (such as Boger fluids) are not prone to reverse swell at all, or if it is simply not experimentally noticeable. For example, Chai and Yeow [22] studied the shape of jets of a Boger fluid and found a small widening at the base, although the bottom boundary condition was somewhat different from here: the jet was falling straight into a pool of the same liquid and was not subject to buckling. Testing the mechanism described in this section would require using another wormlike micellar fluid (different from CPyCl) but with comparable features of significant elasticity, especially large elastic component of extensional stress, and moderate or low viscosity.

2.3. Scaling laws for folding dynamics

Next, we seek to investigate the folding motion of CPyCl wormlike micellar jets. The goal is to understand why this in-plane jet motion (never observed for cylindrical jets of Newtonian fluids) is possible for this shear-thinning viscoelastic fluid. In addition, we derive scaling laws for the folding amplitude L and frequency f that will be compared to experimental measurements.

2.3.1. Mechanism of folding

The mechanism of folding of CPyCl wormlike micellar solution has different roots from Newtonian coiling. Even when the jet is pushed sideways, experimental observations show that it remains relatively straight (Fig. 5(a)), whereas Newtonian jets get bent and twisted over a significant height from the bottom plate. This is allowed by the shear-thinning properties of the fluid, which limit the shear stress in the curved region, as shown in Fig. 5(c), and it is likely that some variant of shear banding takes place in this region. The shear stress $\eta(\dot{\gamma})\dot{\gamma}$ in the curved region is bounded by the plateau stress η_0/λ, regardless of the curvature, whereas it scales with the curvature squared in the Newtonian case (Eq. (8)). The point of contact of the jet with the lower layer of fluid can therefore be in line with the centerline of the jet, and move at the same pace as the rest of the jet. Since it is not twisted the jet does not coil and follows a straight motion.

As the jet translates further and further sideways, the weight of the inclined jet tends to provide a restoring force directed towards the vertical axis. This creates a bending torque within the jet, and it is resisted by a viscous torque that appears when the lower part of the jet bends (Fig. 5(d)). When the lateral displacement reaches its maximum amplitude L, the gravitational torque becomes larger than the viscous torque, and the jet buckles back toward the center line. Such a situation is shown in Fig. 5(b). The jet then makes a new contact point with the layer of liquid, continues its movement because of the steady incoming flow of new fluid from above, and the process repeats itself.

In order to derive scaling laws for the amplitude L and frequency f of folding we have to analyze what happens at the extremal point of this motion. This analysis is similar to the scaling laws developed in Skorobogatiy and Mahadevan (2000) [23] for viscous sheets (i.e. planar jets), except that here, the fact that the jet is straighter, changes the relevant scales.

2.3.2. Connection between amplitude and frequency

In order to connect the frequency of folding to the amplitude we need to obtain an equation for conservation of volume similar to Eq. (7). In contrast to the coiling jet, shown in Fig. 2(a), the radius of the jet during the folding motion is not constant in the bent part, as can be seen in Fig. 5(a). The small horizontal velocity U_3 can be roughly estimated as the horizontal component of $U_2 = Q/\pi a_2^2$: it is approximately zero when the jet is vertical, and largest when it approaches L. Taking an average over one period, we find that this velocity scales as $U_2 a_2/L$. As a result f and L are linked by

$$fL \sim U_2 \frac{a_2}{L} \Rightarrow f \sim \frac{Q}{L^2 a_2} \tag{32}$$

Various regimes exist depending on which force dominates in the jet. The possible driving forces are either viscosity (V), gravity (G), or inertia (I). The resisting force is always viscous. Table 1 summarizes the scaling laws for frequency as a function of H^* and Q^* for the coiling motion in viscous Newtonian fluids, folding motion in viscoelastic fluids, and the scaling laws for the CPyCl solutions obtained via experiments. In the subsequent analyses the dominant force in each regime will be identified via the appropriate subscripts V, G, or I to the frequencies and amplitudes.

2.3.3. Viscous regime

Analogous to Newtonian fluids, at low heights of fall, the driving force for folding is the viscous stress in the fluid near the nozzle. As in the case of viscous coiling, the range of heights of fall for viscous folding will be limited by both the buckling height of the column and transition to gravitational folding. In the cases where viscous folding occurs, no gravitational stretching occurs, so $a_0 = a_1 = a_2$. In this regime the jet amplitude is geometrically constrained by the nozzle-plate distance H, which means that

$$L_\mathrm{V} \sim H \tag{33}$$

The expression for the viscous folding frequency is found using Eq. (32):

$$f_\mathrm{V} \sim \frac{Q}{H^2 a_0} \tag{34}$$

In the viscous regime the motion of the jet is therefore totally constrained by the external parameters of the experimental setup, rather than by the fluid properties.

2.3.4. Gravitational regime

For larger heights of fall, the driving torque is the gravitational torque acting on an arm given by the extremal lateral displacement L This torque scales as

$$T_{\text{driving}} \sim \rho g H a_1^2 L_G \tag{35}$$

At the maximum amplitude L the jet falls backward, bending on the length scale l_{VG}, typical of the opposing influences of gravity and viscosity. The typical curvature of the jet just at that moment is of the order of $\kappa = 1/L$. This leads to local shearing deformation within the curved region of the column, with viscous stresses developing between the outer region (of larger velocity) and the inner region. In this situation, the viscous stress τ_{xz} is the direct analog of the elastic stress in beam bending: it vanishes in the middle of the jet and increases linearly outwards throughout the cross-section. Following this analogy in the fashion developed in [23], the stress is found to be:

$$\tau_{xz} = \eta_0 \dot{\gamma} \sim \eta_0 x \dot{\kappa} \sim \eta_0 \frac{x}{L_{\text{G}}} \frac{Q}{a_1^2 l_{\text{VG}}} \tag{36}$$

Note that at the very onset of bending, the liquid is not sheared, therefore the zero-shear viscosity is used. As expected, the viscous force $d^2F_{\text{V}} = \tau_{xz} dxdy$ integrated over the jet cross-section vanishes. The elementary viscous torque, $\delta^2 T_{\text{V}} = x\tau_{xz} dxdy$, nevertheless, remains non-zero after integration. Approximating the cross-section to a square, the resulting torque is

$$T_{\text{resisting}} \sim \int_{-a_1}^{a_1} \int_{-a_1}^{a_1} x\tau_{xz} dxdy = \eta_0 \frac{a_1^2 Q}{l_{\text{VG}} L_{\text{G}}} \tag{37}$$

The balance between the two torques gives the scaling law for the amplitude of folding

$$L_{\text{G}} \sim \left(\frac{\nu_0 Q}{l_{\text{VG}} g H} \right)^{1/2} \tag{38}$$

In dimensionless form, we obtain the following expression

$$L_{\text{G}}^* \sim \left(\frac{Q^*}{H^*} \right)^{1/2} \tag{39}$$

The expression for a_2 in Eq. (32) is found using Eq. (27), which leads to a dimensionless expression for the frequency in this regime:

$$f_{\mathrm{G}}^{*} \sim \frac{\left(Q^{*5} H^{*}\right)^{1/6}}{a_0^{*2/3} L_G^{*2}} \tag{40}$$

Eliminating the amplitude using Eq. (38), we can derive the following expression for the dimensionless folding frequency in the gravitational regime:

$$f_{\mathrm{G}}^{*} \sim \frac{1}{a_0^{*2/3}} \left(\frac{H^{*7}}{Q^{*}}\right)^{1/6} \tag{41}$$

The transition between viscous and gravitational regimes takes place for $\beta = H a_0 \sqrt{g/6Q\nu} > \pi/2$. For the CPyCl 100 wormlike micellar solution (described in detail below), with $a_0 = 1.25$ mm and $Q = 3$ mL/min, this is equivalent to $H = 3.3$ cm. Once again, at low flow rates, the jet may transition directly from steady flow to gravitational folding.

2.3.5. Inertial regime

In contrast to the inertial regime for coiling ([8], [10]), the type of inertia that drives folding is not the centrifugal (rotational) inertia but the linear, axial inertia. The fluid in the jet tends to travel along a vertical path, which provides a restoring force returning the folded part of the jet toward the center. The inertial force per unit length is $\rho Q^2/a_1^2$, which leads to a torque that scales as

$$T_{\mathrm{driving}} \sim \frac{\rho L_{\mathrm{I}} Q^2}{a_1^2} \tag{42}$$

In this regime the length of the bent region is much smaller than for the gravitational regime, and scales with L rather than l_{VG}. This leads to a viscous torque that scales as

$$T_{\mathrm{resisting}} \sim \eta_0 \frac{a_1^2 Q}{L_{\mathrm{I}}^2} \tag{43}$$

This leads to a folding amplitude that scales as

$$L_{\mathrm{I}} \sim \left(\nu_0 \frac{a_1^4}{Q}\right)^{1/3} \tag{44}$$

In dimensionless terms and using Eq. (26), this can be written in the form

$$L_{\mathrm{I}}^{*} \sim \left(\frac{Q^{*}}{H^{*2}} \right)^{1/3} \tag{45}$$

The volume conservation condition, Eq. (40), is once again used to obtain the scaling law for the folding frequency:

$$f_{\mathrm{I}}^{*} \sim \frac{H^{*3/2} Q^{*1/6}}{a_0^{*2/3}} \tag{46}$$

The inertial regime is expected to appear at large heights, of the order of heights required to have $\rho Q^2/a_1^2 \sim \rho g H a_1^2$; with CPyCl 100 fluid parameter values, that height corresponds to $H \approx 9\nu_0^2/(g l_{VG}^2) = 26.5$ cm. At these heights, thermal effects due to the evaporative cooling of water can also become very important and dramatically alter the viscosity. For this reason, no systematic quantitative measurement has been conducted in this regime.

3. Experimental procedure

3.1. Fluid formulations

The main focus of the study is the behavior of jets of wormlike micellar solutions. In addition, we use a silicone oil as a reference fluid to facilitate qualitative comparison with a viscous Newtonian fluid.

The type of fluids we use for this study are solutions of CPyCl and NaSal in brine (100 mM of NaCl salt solution). Following the study in [20], a fluid in the desired range of viscosity and elasticity is obtained with the concentrations [CPyCl] = 100 mM, and [CPyCl]:[NaSal] = 2:1. For the sake of comparison, two other fluids were prepared with the same brine and the same [CPyCl]/[NaSal] ratio, but [CPyCl] = 75 mM and [CPyCl] = 150 mM, respectively. The three fluids will be denoted as CPyCl 100, CPyCl75, and CPyCl150, respectively, in the rest of the study. CPyCl and NaSal were obtained in dry form from MP Biomedicals, and Sigma-Aldrich, respectively.

As a comparison fluid with Newtonian properties, we used a silicone oil T41 from Gelest Inc.

3.2. Rheological characterization

3.2.1. Shear Rheology

The linear viscoelastic tests were performed on all fluids on a stress-controlled ARG2 rheometer, in a cone-plate geometry of 40 mm diameter, at 22.5^{o}C. We obtain the values of important fluid parameters such as the zero-shear rate viscosity η_0 and the characteristic relaxation time λ, which are summarized in Table 2. The CPyCl solutions exhibit a strong viscoelastic behavior, which is well characterized by small-amplitude oscillatory experiments at low frequencies. A single-mode Maxwell model fits the data well as shown in Fig. 6(a). The relaxation time λ in this model is directly related to the characteristic time of the stress relaxation processe in wormlike micellar solution, as shown in Eq. (12). All the CPyCl solutions are also strongly shear-thinning (Fig. 6(b)), which translates into a critical stress or plateau shear stress (in Fig. 6(c), we show the example of CPyCl 100). This plateau stress corresponds to a stress level that is sufficient to break the weak intermolecular bonds holding the surfactant molecules in the wormlike micelles, leading to their breakup in smaller aggregates. This apparent strong shear-thinning, with $\eta \sim 1/\dot{\gamma}$, can also indicate the onset of shear banding, as predicted by Spenley and co-workers [24], and verified by Berret and co-workers [25]. As we show in Fig. 6(b), below a critical shear rate of the order of $\dot{\gamma}_c \simeq 1/\lambda$, CPyCl solutions show a plateau or zero-shear-rate viscosity (reported in Table 2).

Another non-Newtonian effect is the first normal stress difference that arises because the shear flow tends to deform and align the wormlike micellar network, which leads to a streamline tension resulting in a normal stress difference [26]. In Fig. 6(c), we show that the first normal stress difference increases approximately linearly with the shear rate over the measured range. At low shear rates ($\dot{\gamma}_c \ll 1/\lambda$), where the first normal stress difference is expected to scale quadratically with the shear rate [26], the measured value are below the sensitivity threshold of the ARG2 rheometer.

3.2.2. Extensional rheology

In Fig. 7(a), we show a sequence of snapshots of a typical CaBER experiment conducted on a CPyCl 100 solution. The diameter of the plates is 6 mm, and they are initially separated by 1.2 mm. A step-strain is imposed, pulling the plates apart in 50 ms to 4.8 mm, which represents a Hencky strain $\epsilon = \ln(4.8/1.2) = 1.4$.

As we show in Fig. 7(b), the three solutions behave in a qualitatively different manner in this experiment. CPyCl 75 has such a small viscosity that it almost immediately enters a regime of elasto-capillary exponential thinning. At the other end of the spectrum, CPyCl 150 is almost gel-like, and the liquid filament is sustained for an extended period of time. Breakup eventually occurs, but usually not at the mid-plane [20], thus the typical analysis used in CaBER is not applicable. The CPyCl 100 fluid shows the most interesting behavior with strong non-Newtonian effects.

The first part of the thinning is dominated by a balance between capillary and viscous effects. The mid-plane diameter decreases linearly in time. As this diameter decreases, the extension rate increases, until it starts triggering non-Newtonian effects. The wormlike micelles become increasingly aligned by the extensional flow, building up elastic stresses, which lead to extension-thickening. In Fig. 7(c), we show the first normal stress difference $\tau_{zz} - \tau_{rr}$ as a function of time (scaled by λ) for the three fluids. The main feature exhibited by each fluid is the strong extension thickening as seen from the rapid rise in the first normal stress difference beyond the Newtonian regime. More extensive and detailed studies of capillary thinning experiments with wormlike micellar solutions are discussed by [20] and [27].

3.3. Temperature dependence

The rheological properties of wormlike micelles solutions are highly temperature dependent, for two reasons. The first reason is that the two characteristic timescales of the relaxation processes, λ_r and λ_b evolve with temperature. Here, λ_r refers to the reptating motion of the chain segments and λ_b represents a thermally-activated breakup process. Everything else held constant, both decrease exponentially with temperature. The second source of temperature dependence is the variation of the characteristic length of the micelles, which are dynamic structures. Their average length depends exponentially on the thermally-activated processes of association/dissociation of the surfactant molecules at the ends of the micelles [19]. This affects λ_r through a power law dependence according to the reptation theory of de Gennes [18]: if we denote the characteristic entanglement length of the micelles as L_e, λ_r scales as $L_e^{3.4}$. The temperature dependence of each timescale contributes towards the temperature dependence of λ, the Maxwell model fit parameter for the small angle oscillatory stress data, through the connection given by Eq. (12).

The temperature dependence of λ can be fitted with an Arrhenius equation of the form

$$\lambda(\mathrm{T}) = \lambda_{\mathrm{T}} = \lambda_{\mathrm{Tref}} \exp\left(\frac{\Delta \mathrm{H}}{\mathrm{R}}\left(\frac{1}{\mathrm{T}} - \frac{1}{\mathrm{T}_{\mathrm{ref}}}\right)\right) \tag{47}$$

The ratio $\lambda_{\mathrm{T}}/\lambda_{\mathrm{Tref}}$ is called the shift factor, denoted by a_{T}. In Fig. 8(a), we show that the temperature dependence of the shift factors $a_{\mathrm{T}} = \lambda_{\mathrm{T}}/\lambda_{\mathrm{Tref}}$ with $T_{\mathrm{ref}} = 21.5°\mathrm{C}$ follows the Arrhenius model with a very large activation energy. This in turns leads to a large temperature dependence of the viscosity of the fluid.

As a first approximation, the viscosity of a viscoelastic fluid such as CPyCl 100 is related to its elastic modulus and longest relaxation time by $\eta_0 = G_0\lambda$. Provided that the length of the micelles is long enough for them to entangle, the elastic modulus depends mostly on the surfactant concentration; $G_0 \sim \nu_e k_b T$, where ν_e is the number density of the entanglements. Rubber elasticity theory suggests that G_0 varies only linearly with temperature [28]. An estimate of G_0, the norm of the complex modulus $|G^*| = \sqrt{G'^{\,2} + G''^{\,2}}$, is indeed found to be approximately constant with temperature, as can be seen on the right-hand side of Fig. 8(b). As a result, the zero-shear-rate viscosity of the solution varies exponentially with temperature. This is found to be true experimentally, with an exponential factor of the same order as the elastic relaxation time. The viscosity of the CPyCl 100 solution drops from 25.2 Pa.s at 20°C to 9.3 Pa.s at 25°C. This means that in order to get meaningful experiments with this type of fluid, the temperature must be either carefully controlled, or measured for each experiment in order to correct and re-evaluate the fluid properties in accordance with Eq. (47). Another affect of the temperature can be seen in capillary breakup and filament stretching experiments, as well as during the breakup of the jet falling on a plate at very low flow rates. In these cases, the liquid, initially transparent at ambient temperature (22-23°C), becomes increasingly turbid. Direct temperature measurement with a thermocouple immersed in the small mound of white liquid falling on the bottom plate shows that its temperature can be as low as 16°C. This suggests that the turbidity is caused by the Krafft transition, i.e. the precipitation of surfactant from the solution when the temperature becomes lower than a critical temperature called the Krafft temperature [29]. The Krafft temperature can be measured either by visual observation of turbidity or by the drastic change in most physical properties when the precipitation occur. Figure 8(b) offers one example of such a measurement, with

the abrupt change of the slope of the norm of the complex modulus $|G^*|$ as a function of T in a small angle oscillatory shear test. This leads to an estimate of the Krafft temperature for CPyCl 100 of 18.0^oC, which is consistent with estimates from direct visual observations.

The cooling in itself is likely due to the evaporative cooling of water, which has a strong effect on the temperature of thin filaments because of their divergent surface area to volume ratio. The smaller radius also increases the local capillary pressure, which in turn makes the chemical potential of the solvent higher and accelerates evaporation. Another possibility connecting evaporation and visual appearance of turbidity could simply be that the filament dries, leaving only solid surfactant. These extreme cooling and drying effects tend to appear only the limit of very large jet heights and low flow rates (for example $H = 25$ cm, $Q = 2$ mL/min). The evaporation-driven cooling and concentration increase leads to a large increase in viscosity when the residence time of a fluid particle in the jet becomes of the order of the typical time for the temperature change to take place. In other words, as the height of fall increases and the flow rate decreases, the variability in the local viscosity increases.

The silicone oil shows the typical features of a purely Newtonian fluid, with a constant viscosity. It is a fairly viscous fluid, with values of viscosity similar to those of CPyCl 100, which make it suitable for jetting experiments.

3.4. Experimental setup for jet analysis

Two setups were used for the jetting studies in this research. The first setup simply involves the fluid being pumped by a syringe pump to a nozzle, from where the jet falls onto a plate. Direct observation of the jet profile and dynamics is sufficient to obtain the flow regime, and a video camera is used for quantitative measurements. The second setup is a different view configuration, where we use a laser projected along the fluid column, which helps in precise evaluation of the motion of the jet. Advantages and disadvantages of each method are discussed below. We also discuss the precise definition and possible variants of the bottom plate condition.

3.4.1. Direct observation

The fluid is pumped by a Stoelting syringe pump (Stoelting 53130) with a controlled flow rate. The fluid is placed in a 60 mL syringe, and a flexible plastic tube is attached to it. The other end of the tube has a nozzle attached to it, through which the fluid exits as a jet. The nozzle is attached to a

vertical-axis linear stage, and the liquid falls onto a plate below the nozzle (see Fig. 9(a)). The plastic tube is approximately 20 cm long, which implies that the residence time of fluid particles in the tube is between 10 and 20 seconds, greatly exceeding the relaxation times listed in Table 2. This ensures the relaxation of any stress occurring at the exit of the syringe. We mostly report results obtained with a circular nozzle of diameter $a_0 = 1.25$ mm, but the influence of the nozzle radius has also been investigated with two additional sizes, $a_0 = 0.775$ mm and $a_0 = 2.40$ mm. The motion of the jet was recorded using a BlueFox digital videocamera at frame rates from 30 to 50 fps. Frequency measurements were done by frame counting, and amplitude measurement were done using the image analysis software ImageJ, using an image of a ruler as reference. A high-speed videocamera (Phantom V from Vision Research) was also used to capture rapid phenomena such as jet breakup and the Kaye effect, at frame rates from 500 to 800 fps.

3.4.2. Trajectory tracking with laser

A second setup was used to follow the trajectory of the jet, inspired from an experimental technique used by Versluis [30] to study the Kaye effect. A red He-Ne laser beam shines through the jet using a T-shaped nozzle and is guided along the jet like in an optic fiber (Fig. 9(b)). The camera records the position of the beam spot through the transparent bottom plate, using a mirror at a 45° angle. An image analysis code then evaluates the precise position of the spot. The technique allows for the quantitative understanding of the trajectory of the jet in folding motion, including tracking over many periods that reveals the stability of the folding regime. The shortcomings of this technique are that the liquid jet is an imperfect waveguide, and therefore allows the laser beam to be transmitted through the free surface of the jet when the angle of incidence is too large, which happens at large amplitude. Conversely, at very small amplitudes of the jet motion changes in the position of the laser spot are smaller than the size of the spot and hence difficult to quantify.

3.4.3. Discussion of the bottom-plate condition

Two questions regarding the bottom-plate conditions must be addressed to ensure that the problem is correctly defined. First of all, the jet does not fall directly on the plate, but on a thin layer of fluid that is covering the plate. We are only interested here in steady state regimes, for which the jet falls on a layer of fluid, as opposed to the initial transients when the jet falls on the

clean plate. The thickness of this layer is "chosen" by the fluid, to balance the viscous stresses between the upper, free layer and the no-slip plate-fluid interface, with the incoming flow rate. This thickness is taken into account in the measurement of the height of fall, which is defined as the distance between the fluid layer and the nozzle. The spreading fluid is either allowed to collect into in a secondary reservoir when it reaches the end of the plate, or the plate is cleaned before being the next run.

The second point to note is that other geometries beyond the flat plate could be envisioned, which may be relevant for industrial applications. The jet could fall on a bath of the same or of a different fluid, on an inclined plane, or on a curved surface. Different plate sizes could also influence how fast the fluid layer drains into the secondary reservoir. In the present study, we are interested in planar geometries. The drainage mechanism does not play a significant role, because of the fact that the layer thickness is taken into account for the measurement of the height of fall, and the short duration of the measurement. The liquid bath, in the end, is the only alternative that could lead to dramatically different behavior such as air entrainment [31], at least for large incoming speed. Nevertheless, for the moderate jet speeds involved in most parts of the parameter space studied in this paper, all phenomena of interest occur on timescales shorter than the spreading time for the viscous fluids used. As a result, the jet motion studied in our experiments always occurs on a small mound of fluid that has not spread completely.

3.5. Experimental results

We first begin by a qualitative description of the different jetting regimes involved, which are mapped onto the parameter space described earlier. This helps in understanding what experimental conditions are required for the novel regimes of CPyCl solution jets to take place. Then, we investigate quantitatively the reverse swell and folding phenomenon, and the results are compared to theoretical predictions.

3.5.1. Regime maps

We map the different jetting regimes for the Newtonian silicone oil (see Fig. 10(a)) and for the wormlike micellar solution CPyCl 100 (see Fig. 10(b)). The maps presented in Fig. (10) are drawn in the dimensionless ($Q^* = Q(g/\nu^5)^{1/3}$, $\epsilon = H/2a_0$) parameter space. The scaling of Q^* allows for comparisons with different fluid viscosities, which is especially important for

comparing experiments with CPyCl solutions conducted at different ambient temperatures. The choice of ϵ as a relevant dimensionless height is due to the fact that the predictions for jet buckling (Eqs. (2) and (3)) use this geometrical parameter. Nevertheless, the other dimensionless height $H^* = H(g/\nu^2)^{1/3}$ becomes more relevant when the focus is on large-height behavior.

Steady jet

In this regime, the jet is steady over time, and the fluid spreads at a uniform rate on the plate. This regime occurs when the jet is not buckled, which means at low heights of fall, and is similar for all the test fluids. This flow state is commonly known as the stagnation slow.

Non-continuous jets

In this regime, which occurs at low flow rates and moderate heights, the jet is non-continuous. This means, for the Newtonian silicone oil, that the fluid will *drip* from the nozzle rather than form a jet, or form a jet that periodically breaks under the effect of surface tension. For viscoelastic fluids with large extensional viscosity such as the CPyCl solutions, it may also mean the formation of persistent thinning filaments between the nozzle and the plate with beads of fluids periodically sliding down the filament. This transient situation is a direct application of CaBER experiments, and is also reminiscent of the beads-on-a-string [32] and gobbling phenomena [33].

Coiling

Coiling is the typical mode of motion for buckled jets of Newtonian fluids. As reported in the regime map of Fig. 10(b), jets of CPyCl solutions can also show coiling, although the range of experimental parameters for which it happens is more limited than in the Newtonian case. In addition, the shape and curvature of coiling jets of CPyCl jets (see Fig. 4(c)) is different from their Newtonian counterpart (see Fig. 1(c)) and the equations for Newtonian coiling may not apply.

Folding

The folding regime of CPyCl jets is studied in detail because it is qualitatively different from the dynamical motion of Newtonian jets. In Fig. 11,

we show two snapshots of the same jet of CPyCl 100 at different instants during a folding period. In Fig. 11(a), we show the jet when it is almost vertical, whereas in Fig. 11(b) the lateral jet displacement is at its maximum amplitude L and is about to fall back. In addition, in Fig. 11(c), we show an example of the jet trajectory obtained by the laser tracking system. One can see the oscillatory motion is confined primarily to a fixed plane, thus justifying the concept of folding. We can also see the events of coiling, that occurs when the fluid builds up a secondary mound from which the jet tends to be deflected. Nevertheless, after two coils, the jet returns spontaneously to its folding motion, because this regime is more stable under these specific experimental conditions.

Bistable regime

In this regime the jet either coils or folds, depending on the history of the flow and the boundary conditions at the bottom plate. Small perturbations such as the presence of a heap of fluid on the bottom plate can trigger the switch between the regimes. In this case both regimes are stable and the system can be forced from one to another. In the same way coiling jets of Newtonian fluids can also display bistable states over a limited range of impact height or flow rate.

High-flow-rate ductile failure

At large flow rates and high extension rate, micellar fluids tend to break in a rubber-like ductile failure [16]. This happens when the weight of the fluid column pulling on a particular cross-section of the jet, usually close to the nozzle, becomes larger than the stress the micelles can sustain. As a result, the micelles break locally, leading to a local weakening of the jet, in turn leading to rupture of the entangled micelles. This creates a fracture pattern reminiscent of rubber failure in solid mechanics, as can be seen in Fig. 12. The dynamics of this ductile pinch-off for a micellar network have been considered by Cromer et al. [34].

3.6. Comparison of the regime maps

Figure 10(a) shows the regime map for the viscous Newtonian oil (silicone oil T41), for which only three regimes are typically observed: steady jetting, dripping, and coiling. Note that sub-classification of coiling in viscous, gravitational and inertial regimes is not taken in account here, since it is hard

to determine without actually measuring the coiling frequency. This can be done by frame counting using the setup of Fig. 9(a) and has already been performed in the studies by Ribe [10]. The buckling transition at moderate flow rates is consistent with Eq. (2) (dashed line). At large flow rates, the increased compressive stress favors buckling, and the transition happens at a lower height.

The dripping-jetting transition (solid line) is observed to obey the scaling law $\epsilon \sim Q^{*1.7}$. Using Eq. (14) and Eq. (15), we find that the flow rate required to maintain a continuous jet increases with height of fall and scales as

$$Q \sim H^{1/1.7} \simeq H^{0.6} \tag{48}$$

Figure 10(b) shows the corresponding experimental regime map for CPyCl 100. Several features can be noted in comparison to the Newtonian diagram. Some features are somewhat similar to the Newtonian regime map; a stable axisymmetric jet is maintained at low heights of fall, and a non-continuous jet develops at low flow rates. Most of the parameter space is occupied by time-dependent buckled jets. Nevertheless, significant changes are also noticeable compared to Newtonian fluids, such as the existence of the folding regime, the ductile failure at large flow rates, the coexistence of bistable folding and coiling regimes, and the different slope of the dripping-jetting transition. Measurements with CPyCl 75 and 150 show a behavior very similar to CPyCl 100 and the corresponding regime maps are not shown here for brevity.

3.7. Experimental scaling laws for the regime transitions of CPyCl solutions

In this section we report detailed investigations of the transitions between different regimes. The experiments are for different CPyCl solutions and experimental conditions (flow rate, height of fall, and nozzle size). In Fig. 13, we present the data for one transition each, with respect to the relevant dimensionless parameters at that transition. The horizontal axis is always $Q^* = Q(g/\nu^5)^{1/3}$, which scales for the effect of viscosity and allows a direct comparison between the different solutions. The vertical axis is either $\epsilon = H/2a_0$ or $H^* = H(g/\nu^2)^{1/3}$, depending on which variable allows for a better collapse of the data set. The column aspect ratio ϵ is expected to be more relevant at low heights, whereas H^* should be the more relevant variable at larger heights, when gravitational thinning takes place. The nozzle radius was corrected to take into account the die-swell observed experimentally [21], which is especially important at large flow rates and small nozzle radii.

Buckling limit

In Fig. 13(a), we show that the jet buckles and starts folding when the aspect ratio $\epsilon \approx 4.8$. This value is in good agreement with the prediction given by Eq. (3), $\epsilon = 4.81$ (solid line). There is a strong hysteresis between the unbuckled and folding regimes when the height of the fall is varied continuously. This explains in part the scatter of the data. Nevertheless, the transition happens for $3 < \epsilon < 8$ when Q^* is varied across three orders of magnitude. Newtonian fluids buckle at a higher value of ϵ, $\epsilon \simeq 7.66$ as given by Eq. (2).

The first Folding-Coiling transition

Above the limit given by Eq. (2), the jet switches to the azimuthal mode of instability and begins to coil. In Fig. 13(b), we show this transition from folding to coiling, which occurs at $\epsilon \simeq 7.66$. This is the limit at which Newtonian jets usually buckle and start coiling. It immediately suggests that the analysis that led to the limits (Eq. (2)) and (Eq. (3)) for the Newtonian fluids is still valid for the CPyCl solutions, although in the case of CPyCl solutions the folding mode is stabilized by mechanisms that do not exist in the Newtonian case. Experiments show that the transition between the folding and coiling occurs over a somewhat broad range of heights for which the two modes alternate; the switching between the two being triggered by random events such as the jet impacting a heap of liquid that has not evenly spread out. Cruickshank [5] also noted this problem in the narrow parameter range where folding was observed with Newtonian fluids. It is interesting to note that when the ambient temperature is closer to 25°C, so that the viscosity is lower, the heaps of liquid are less pronounced, and the frequent switching is replaced by a bistable region (shown in Fig. 10(b)), leading to a large hysteresis in the transition. Overall, there is some scatter around the predicted value of $\epsilon \simeq 7.66$ for this transition, with $4 < \epsilon < 12$, but once again this remains valid over three orders of magnitude for Q^*.

Second Folding-Coiling transition

When the height of fall is raised even more, a second transition occurs, from coiling back to folding, with an even more pronounced bistability than the first transition (see Fig. 10(b)). We measured the transition from coiling to bistable folding and coiling. In other words, starting from a well-developed

coiling state and for a given flow rate, we raised the height until we saw the first events of folding. For this transition, the parameter that allowed the best collapse of the data was the dimensionless height of fall H^* rather than the aspect ratio ϵ. In contrast to the measurements of the previous two boundaries, the critical height for this transition varies with the flow rate. As the flow rate increases over three orders of magnitude, the height at which the transition occurs also increases, but as a power-law. Experimentally, the scaling is close to $H^* \sim Q^{*1/3}$, as shown in Fig. 13(c).

Jet rupture at large flow rate: ductile failure

At very large flow rates, the entangled wormlike micellar network cannot sustain the axial stresses anymore and break *en masse*, leading to the solid-like ductile failure of the jet. The flow rate required to observe jet rupture decreases with height, and scales as $Q^* \sim H^{*-1/1.54} = H^{*-0.65}$, as shown in Fig. 13(d). There is an overlap between the coiling and jet rupture zones, for which the jet has enough time to coil a few times before breaking. Since the weight of the column of fluid is the driving force for this mode of jet breakup, it happens at large flow rates and heights of fall, in the upper-right corner of the stability diagram shown in Fig. 10(b).

Dripping-Jetting transition at low flow rates

We now describe the dripping to jetting transition boundary, which occurs at low flow rates and large heights. Dripping occurs when the height is large enough at a given flow rate such that a continuous jet can not be maintained. Instead of Newtonian dripping and capillary breakup, the non-continuous regime for CPyCl 100 is observed to consist of long, thin filaments, which are prevented from breakup by elastic forces. A significant difference with the Newtonian regime map is that the transition between the non-continuous and continuous jet happens at a constant flow rate, $Q^* > Q^*_{\min}$, for all heights, above a minimum height (see Fig. 10(a) and (b), non-continuous regime). Since it is the elasticity of the entangled micellar network that holds the thread and prevents breakup, a continuous jet is sustained above a threshold flow rate.

3.7.1. Measurements of Jet Radius

For the wormlike micellar fluids, we have shown that the jet radius increases near the plate and the minimum radius is achieved at a certain height

above the plate. In order to measure the amount of swelling with respect to the experimental parameters H^* and Q^*, we use the setup described in Fig. 9(a). We perform three sets of experiments, one with a constant flow rate of $Q^* = 7.1 \times 10^{-5}$, and two sets of complementary experiments with a constant height of fall, with $H^* = 1.7$ and $H^* = 3.4$. The relevant conjugate variable (H^* or Q^*, respectively) was then slowly varied. The measurements are shown in Fig. 14. Here, $a_1^* = a_1(g/\nu^2)^{1/3}$ is the scaled radius of the jet just above the swell, $\alpha = a_2/a_1$ is the swelling ratio, and $h^* = h(g/\nu^2)^{1/3}$ is the scaled height of the swollen region. We compare the experimental values of these parameters to the theoretical predictions of Eqs. (26), (25) and (29), respectively. In Fig. 14(a), we show the jet profile along with the definitions of different length scales. In Fig. 14(b), we show the dimensionless radius just above the swell. In Fig. 14(c), we show the swelling ratio and in Fig. 14(d), we show the height of the swollen region. The data for the different experiments collapse well with the theoretical scaling. The only departure from theory is the value of h^* for one of the data sets, for which the onset of swelling was difficult to detect.

3.7.2. Jet dynamics

The variations of folding frequency f and amplitude L with respect to experimental parameters are presented in Fig. 15. Multiple series of experiments were performed to fully capture the folding dynamics, in two sets. In the first set, three series of amplitude and frequency measurements were made with a fixed flow rate and varying height. The imposed flow rate was $Q = 2$ mL/min for the first two series and $Q = 5$ mL/min for the third one. The series of tests were conducted at different ambient temperatures, 22.5^oC, 20.6^oC, and 21.5^oC, which also affects the viscosity of the fluid, leading to three values of imposed dimensionless flow rates: $Q^* = 4.3 \times 10^{-5}$, $Q^* = 7.1 \times 10^{-5}$, and $Q^* = 1.7 \times 10^{-4}$, respectively. For each series, the flow rate was held constant, while the fall height of the jet was varied from 1.2 to 20 cm ($0.4 < H^* < 6.7$). Note that amplitude data were difficult to collect at low values of H^* and are therefore reported over a smaller range than the corresponding frequency data. In the second set of tests, four series of experiments were performed with a fixed height of fall and varying flow rate. The heights of fall were $H = 5, 6, 9$ and 10 cm (with temperatures of 22.5^oC, 21.3^oC, 21.8^oC, and 22.5^oC, respectively, and dimensionless heights given by $H^* = 1.7, 1.9, 3.2, 3.4$, respectively). The flow rate Q was varied between 0.5 and 9 mL/min ($1.5 \times 10^{-5} \leqslant Q^* \leqslant 2.1 \times 10^{-4}$). All experiments were done

using the CPyCl 100 fluid, because it is better suited for studying continuous jets as discussed earlier and it helps in eliminating other factors affecting the dynamics, especially fluid rheology. The elasto-gravitational number for this fluid at 22.5^oC is $E_g = \lambda\,(g^2/\nu_0)^{\frac{1}{3}} = 12.4$. The high elasto-gravitational number implies that significant elastic effects are expected to occur at fall heights when gravitational thinning is important.

Experimental results and the associated scaling laws are reported in Fig. 15. In Figs. 15(a) and (b), we show the frequency measurements, while in Figs. 15(c) and (d) we show the corresponding amplitude data. Panels (a) and (c) are the first set of experiments with fixed flow rate, while (b) and (d) are the second set with fixed height of fall. Data points for each set of experiments are collapsed using experimental scaling laws obtained from the other set iteratively until self-consistency is achieved. Eventually, the following experimental scaling laws for folding motion are found:

$$\text{For frequency, } f^* \sim H^{*0.66} Q^{*-0.19} \tag{49a}$$

$$\text{For amplitude, } L^* \sim H^{*0.50} Q^{*0.60} \tag{49b}$$

where, as defined in the non-dimensionalization scheme, $H^* = H(g/\nu^2)^{1/3}$, $Q^* = Q(g/\nu^5)^{1/3}$, $f^* = f(\nu/g^2)^{1/3}$, and $L^* = L(g/\nu^2)^{1/3}$.

We note that the power laws in Eqs. (49a) and (49b) are obtained from global regression of all experiments taken together, whereas each series of experiments give scaling exponents that are different from the overall trend. The causes for these variations are difficult to control and result from experimental conditions, such as the effect of temperature on extensional viscosity, the effect of ambient humidity on evaporation and cooling, or rheological aging of the solution. These parameters are constant for a given series of experiments, but vary systematically from series to series, therefore a statistical analysis based on the hypothesis of stochastic deviation from a trend is not applicable. It is only possible to give the range of scaling exponents obtained from different series, which are provided in Table 3. Within this range of uncertainty, theoretical prediction for the folding amplitude and frequency and experimental measurement (all gathered in Table 1) agree.

4. Conclusion

The jetting dynamics of viscoelastic shear-thinning fluids impacting on a plate are qualitatively different from their viscous analog. Cylindrical jets

of CPyCl wormlike micellar solutions falling on a plate from a sufficient height tend to exhibit a folding transition with a periodic oscillating lateral motion. This contrasts with Newtonian fluids for which this folding motion is only observed for planar sheets. We can understand this phenomenon by noting the pronounced shear-thinning of the fluid, which allows a local drop in viscosity at the most curved part of the jet, reducing the local viscous torque. While the Newtonian jets deal with this viscous torque by twisting and coiling out of plane, wormlike micellar jets can remain planar and fold backwards and forwards. Another novel feature of these jets of wormlike micellar fluids is the widening or "reverse swell" at the base. We have shown that this feature can be interpreted in terms of the extensional elastic stress, stored during the stretching of fluid elements in the portion of the jet accelerated by gravity, and partially recovered in the compressive part close to the bottom plate. We have provided scaling laws for these two features that agree broadly with experimental measurements. In addition, we have documented the locations of the different jetting regimes on dimensionless regime maps (see Fig. 10), and studied in more detail the transitions between the different regimes for CPyCl micellar jets.

Many other classes of filling operations exploit jetting of complex fluids. Surfactant-based fluids like Sodium Lauryl Ether Sulphate (SLES) are an important ingredient in many consumer products including shampoos and liquid detergents. Some other consumer products like conditioners, toothpastes, and food products exhibit finite yield stresses. Future work will involve these classes of non-Newtonian fluids to examine the differences in their jetting behavior. For example, in addition to coiling, fluids exhibiting yielding behavior tend to show pronounced mounding [35]. In addition to using different fluids, other possible extensions include a study of the jetting behavior in confined geometries, replicating container filling process [35], and the jetting behavior at higher speeds and consequently higher shear rates, which are closer to actual industrial filling process in terms of the relevant dimensionless operating parameters.

5. Acknowledgements

This research was supported by a gift from the Procter and Gamble Company.

References

[1] B. Pouligny, M. Chassande-Mottin, Air ingestion by a buckled viscous jet of silicone oil impacting the free surface of the same liquid, Phys. Rev. Lett. 100 (2008) 154501.

[2] J. O. Cruickshank, B. R. Munson, The viscous-gravity jet in stagnation flow, J. Fluid Eng. 104 (1982) 360-362.

[3] G.I. Taylor, Instability of jets, threads and sheets of viscous fluid, Proc. 12th Intl. Conf. on Applied Mechanics, Springer, Berlin, 1968.

[4] J. O. Cruickshank, B. R. Munson, Viscous fluid buckling of plane and axisymmetric jets, J. Fluid Mech. 113 (1981) 221-239.

[5] J. O. Cruickshank, Low Reynolds number instabilities in stagnating jet flows, J. Fluid Mech. 193 (1988) 111-127.

[6] B. Tchavdarov, A.L. Yarin and S. Radev, Buckling of thin liquid jets, J. Fluid Mech. 253 (1993) 593-615.

[7] A. L. Yarin and B. M. Tchavdarov, Onset of folding in plane liquid films, J. Fluid Mech. 307 (1996) 85-99.

[8] L. Mahadevan, W S. Ryu and A D.T. Samuel, Fluid rope trick investigated, Nature 392 (1998) 140-141.

[9] L. Mahadevan, W.S. Ryu, A. D. T. Samuel, Correction to "Fluid rope trick investigated", Nature 403 (2000) 502.

[10] N. M. Ribe, Coiling of viscous jets, Proc. R. Soc. London A 460 (2004) 3223-3239.

[11] M. Maleki, M. Habibi, R. Golestanian, N. M. Ribe, D. Bonn, Liquid rope coiling on a solid surface, Phys. Rev. Lett. 93 (2004) 214502.

[12] H. Rehage and H. Hoffmann, Rheological properties of viscoelastic surfactant systems, J. Phys. Chem. 92 (1988) 47124719.

[13] J. N. Israelachvili, D. J. Mitchell, B. W. Ninham, Theory of self-assembly of hydrocarbon amphiphiles into micelles and bilayers, J. Chem. Soc. Faraday Trans. 2 (72) (1976) 1525-1568.

[14] J.P. Rothstein, Strong flows of viscoelastic wormlike micelle solutions, to appear in Rheology Reviews, D.M. Binding and K.Walters eds., The British Society of Rheology, Aberystwyth, Wales, UK, 2009.

[15] B. Yesilata, C. Clasen, G.H. McKinley, Nonlinear shear and extensional flow dynamics of wormlike surfactant solutions, J. Non-Newtonian Fluid Mech. 133 (2006) 73-90.

[16] J.P. Rothstein, Transient extensional viscosity of wormlike micelles solutions, J. Rheology 47 (2003) 1227-1247.

[17] J.-F. Berret, J. Appell and G. Porte, Linear rheology of entangled wormlike micelles, Langmuir 9 (1993) 2851-2854.

[18] P.-G. de Gennes, Simple views on condensed matter, World Scientific, Singapore, 1992.

[19] M. E. Cates, Reptation of living polymers: Dynamics of entangled polymers in the presence of reversible chain-scission reactions, Macromolecules 20 (1987) 2289-2296.

[20] A. Bhardwaj, E. Miller, J.P. Rothstein, Filament stretching and capillary breakup extensional rheometry measurements of viscoelastic wormlike micelle solutions, J. Rheology 51 (2007) 693-719.

[21] R. I. Tanner, Engineering rheology, 2nd ed, 421-435, Oxford Scientific Press, 2000.

[22] M. S. Chai, Y. L. Yeow, Modeling of fluid M1 using multiple relaxation time constitutive equations, J. Non-Newtonian Fluid Mech. 35 (1990) 459-470.

[23] M. Skorobogatiy and L. Mahadevan, Folding of viscous sheets and filaments, Europhys. Lett. 52 (2000) 532-538.

[24] N. A. Spenley, M.E. Cates, T.C.B. McLeish, Nonlinear rheology of wormlike micelles, Phys. Rev. Lett. 71 (1993) 6-9.

[25] J.-F. Berret, D. C. Roux, G. Porte, Isotropic-to-nematic transition in wormlike micelles under shear, J. Phys. II France 4 (1994) 1261-1279.

[26] R. B. Bird, R. C. Amstrong, O. Hassager, Dynamics of polymeric liquids, John Wiley & Sons, New York, 1987.

[27] E. Miller, C. Clasen, J. Rothstein, The effect of step-stretch parameters on capillary breakup extensional rheology (CaBER) measurements, Rheo. Acta 48 (2009) 625-639.

[28] R. G. Larson, The structure and rheology of complex fluids, Oxford University Press, 1999.

[29] PAC, Manual of Symbols and Terminology for Physicochemical Quantities and Units, Appendix II: Definitions, Terminology and Symbols in Colloid and Surface Chemistry, 31 (1972) 613.

[30] M. Versluis, C. Blom, D. van der Meer, K. Van der Weele and D. Lohse, Leaping shampoo and the stable Kaye effect, J. Stat. Mech. P07 (2006) 007.

[31] E. Lorenceau, J. Eggers, D. Quéré, Air Entrainment by a Viscous Jet Plunging into a Bath, Phys. Rev. Lett. 93 (2004) 254501.

[32] M. S. N. Oliveira, G. H. McKinley, Iterated stretching and multiple beads-on-a-string phenomena in dilute solutions of highly extensible flexible polymers, Phys. Fluids 17 (2005) 071704.

[33] C. Clasen, J. Bico, V. Entov, G.H. McKinley, 'Gobbling drops': the jetting/dripping transition in flow of polymer solutions, J. Fluid Mech. 636 (2009) 5-40.

[34] M. J. Cromer, P. L. Cook, G. H. McKinley, Extensional flow of wormlike micellar solutions, Chem. Eng. Sci. 64 (2009) 4588-4596.

[35] A. N. Alexandrou, E. Duc, V. Entov, Inertial, viscous, and yield stress effects in Bingham fluid filling of a 2-D cavity, J. Non-Newtonian Fluid Mech. 96 (2001) 383-403.

Figure Captions

Figure 1: Instabilities of a fluid jet impacting a plate. a) The jet remains axisymmetric at low heights. b) Compressive forces in the jet lead to buckling at a critical aspect ratio. c) Coiling jet. Panels a) and b) are jets of CPyCl, a wormlike micellar fluid, which is described in detail in the text. Panel c) is a silicone oil jet, a Newtonian fluid.

Figure 2: Instabilities in the jet of a Newtonian fluid. a) Coiling jet of Newtonian silicone oil. b) Schematic view of the coiling motion of an axisymmetric jet of Newtonian fluid.

Figure 3: Schematic view of the assembly process of wormlike micelles.

Figure 4: Jets of a wormlike micellar fluid. a) Close-up of the reverse swell for a jet of CPyCl 100 with $H = 6$ cm and $Q = 0.5$ mL/min ($H^* = 1.8$, $Q^* = 1.3 \times 10^{-5}$, $Wi = 11.3$); the measured variables are also indicated. The black bar is approximately 1 cm. b) Snapshot and schematic view of the folding jet of CPyCl 100 with $H = 6$ cm and $Q = 3$ mL/min ($H^* = 1.8$, $Q^* = 8.0 \times 10^{-5}$). c) Snapshot of a coiling jet of CPyCl 100 with $H = 3$ cm and $Q = 5$ mL/min ($H^* = 0.9$, $Q^* = 1.3 \times 10^{-4}$).

Figure 5: Different views of folding mechanism. a) A CPyCl jet at the farthest position. b) Schematic view of the folding mechanism: the jet tends to fall vertically under its own weight, which is resisted by a viscous torque. c) At the farthest position of the oscillation, just at the onset of buckling of the main part of the jet under the weight of the jet, the fluid is not sheared, whereas the contact zone with the fluid layer is in highly shear-thinning or shear-banding conditions. d) Close-up of the buckled region of the jet, in which curvature induces shear stress τ_{xz}.

Figure 6: Rheological properties of micellar solutions. a) Small amplitude oscillatory test of CPyCl 100, fit by a single-mode Maxwell model (similar fits were found for CPyCl 75 and CPyCl 150). Here, $\lambda = 0.72$s, and $G_0 = 26.04$Pa. b) Steady shear viscosity of CPyCl 75 (▲), CPyCl 100 (■) and CPyCl 150 (●), as a function of shear rate. c) Steady shear first normal stress difference as a function of shear rate.

Figure 7: Capillary Breakup Extensional Rheology (CaBER) experiments, with plates of 6 mm diameter and an imposed Hencky strain of 1.4. a) Side view of an experiment with CPyCl 100 ($\tau_{Break} = 15.8$ s). b) Evolution of the diameter with time scaled by the solution relaxation time measured in shear and reported in Table 2, for CPyCl 75, 100, and 150. Each solution behaves in a qualitatively different fashion. c) First normal stress difference for the

same three fluids.

Figure 8: Temperature dependence of the viscometric properties of CPyCl 100 micellar solution. a) Shift factors with $T_{ref} = 294.65\ K$. b) Krafft transition at $T = 18^oC$ shown as change of slope of the complex modulus $|G^*| = \sqrt{G'^2 + G''^2}$ as a function of T, in an oscillatory shear experiment at a frequency of $\omega = 1\ s^{-1}$.

Figure 9: Experimental setups. a) Experimental setup for regime diagram and quantitative measurements. b) Experimental setup for trajectory visualization.

Figure 10: Experimental regime maps for silicone oil (Panel a) and CPyCl 100 (Panel b) in the $\epsilon = H/2a_0$ and $Q^* = Q(g/\nu^5)^{1/3}$ space. a) The silicone oil shows only three behaviors in the ranges of heights and flow rates investigated: steady jet (▲), dripping (□), and coiling (●). b) CPyCl 100 also shows folding (■), bistable coiling and folding (⌀), elastic rupture (★). Solid lines are guide to the eye for regime transitions, while the dashed lines are Cruickshank's prediction for buckling transition (2) and (3).

Figure 11: Different views of the folding motion. a) Folding jet as it reaches the central vertical position. b) The same jet at its farthest lateral displacement, at the onset of buckling under the jet's weight. c) An example of the trajectory of the laser spot (viewed from below), for a jet of CPyCl 100, from a height H = 11.4 cm ($H^* = 3.86$), with a flow rate Q = 3 ml/min ($Q^* = 1.06 \times 10^{-4}$). The values of the Reynolds and Ohnesorge number Re $= 10^{-3}$ and $Oh^2 = 10^{-4}$ are typical of the jetting experiments in this paper.

Figure 12: Successive views of the high-flow-rate rupture of a jet of CPyCl 100, at $H^* = 4.8$ and $Q^* = 2.7 \times 10^{-4}$ ($H = 16$ cm, $Q = 10$ mL/min). a) Onset of the ductile failure. All snapshots are separated by $\delta t = 24$ ms, which corresponds to $\delta t/\lambda = 0.033$.

Figure 13: The transitions between different flow regimes with CPyCl 100 and $a_0^* = 2.6 \times 10^{-2}$ (■); CPyCl 75 and $a_0^* = 4.2 \times 10^{-2}$(●); CPyCl 100 and $a_0^* = 4.2 \times 10^{-2}$(▲); CPyCl 150 and $a_0^* = 4.2 \times 10^{-2}$(⧫); and CPyCl 100 and $a_0^* = 8.1 \times 10^{-2}$(▼). a) The critical condition for transition between steady axisymmetric flow and folding (buckling) at $\epsilon = 4.8 \pm 2$ b) Transition from folding to coiling when the height of fall is increased from a low height for a given flow rate at $\epsilon = 7.6 \pm 1$ c) Transition from folding to coiling when the height of fall is decreased from a large height for a given flow rate. d) Appearance of jet rupture event when increasing flow rate for a given height of fall.

Figure 14: Quantitative measurements of the dynamics in the tail. Here,

$Q^* = 7.1 \times 10^{-5}$, $0.4 \leqslant H^* \leqslant 6.8$ (▲); $H^* = 1.7$, $2.8 \times 10^{-5} \leqslant Q^* \leqslant 3.2 \times 10^{-4}$(•); and $H^* = 3.4$, $2.8 \times 10^{-5} \leqslant Q^* \leqslant 2.1 \times 10^{-4}$(■). a) Definitions of the measured variables. For this jet $H^* = 2.4$, $Wi = 29.8$. b) Dimensionless radius just above the swell. c) Swelling ratio $\alpha = a_2/a_1$ d) Height of the swollen region.

Figure 15: Quantitative measurements of folding properties, frequency (a and b) and amplitude (c and d). The first set of experiments with fixed flow rate (a and c): $Q = 2$ ml/min ($Q^* = 4.3 \times 10^{-5}$) (•); $Q = 2$ ml/min ($Q^* = 7.1 \times 10^{-5}$) (■); $Q = 5$ ml/min ($Q^* = 1.7 \times 10^{-4}$) (▲). The second set of experiments with fixed height of fall $H = 5$ cm ($H^* = 1.7$) (○); $H = 6$ cm ($H^* = 1.9$) (□); $H = 9$ cm ($H^* = 3.2$) (△); $H = 10$ cm ($H^* = 3.4$) (▽).

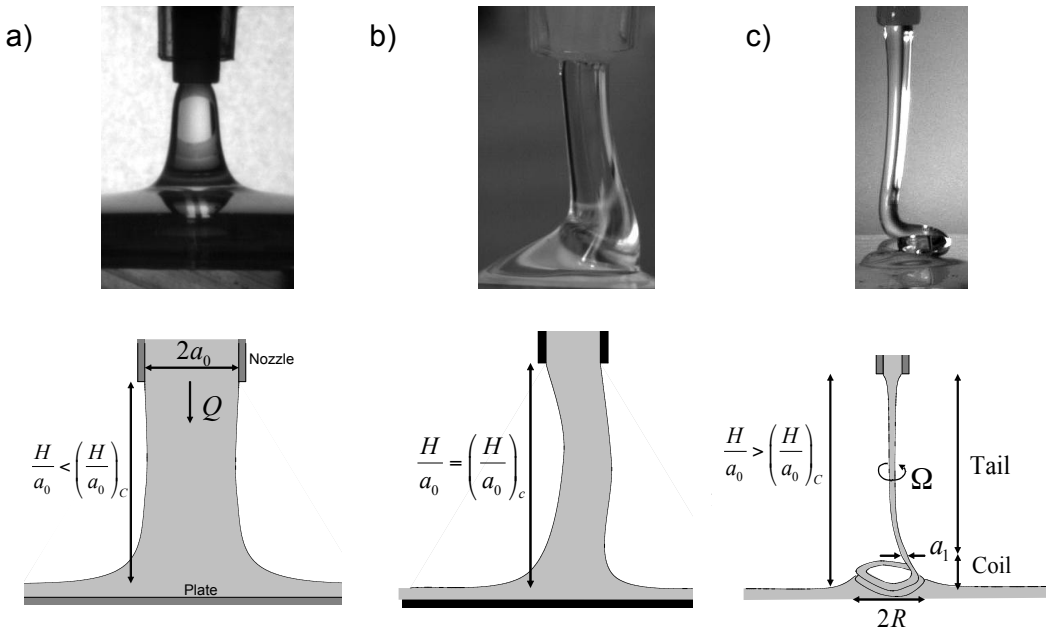
a)
b)
c)
$2a_0$
Nozzle
Q
$\frac{H}{a_0} < \left(\frac{H}{a_0}\right)_C$
Plate
$\frac{H}{a_0} = \left(\frac{H}{a_0}\right)_c$
$\frac{H}{a_0} > \left(\frac{H}{a_0}\right)_C$
Ω
Tail
a_1
Coil
$2R$

Fig. 1

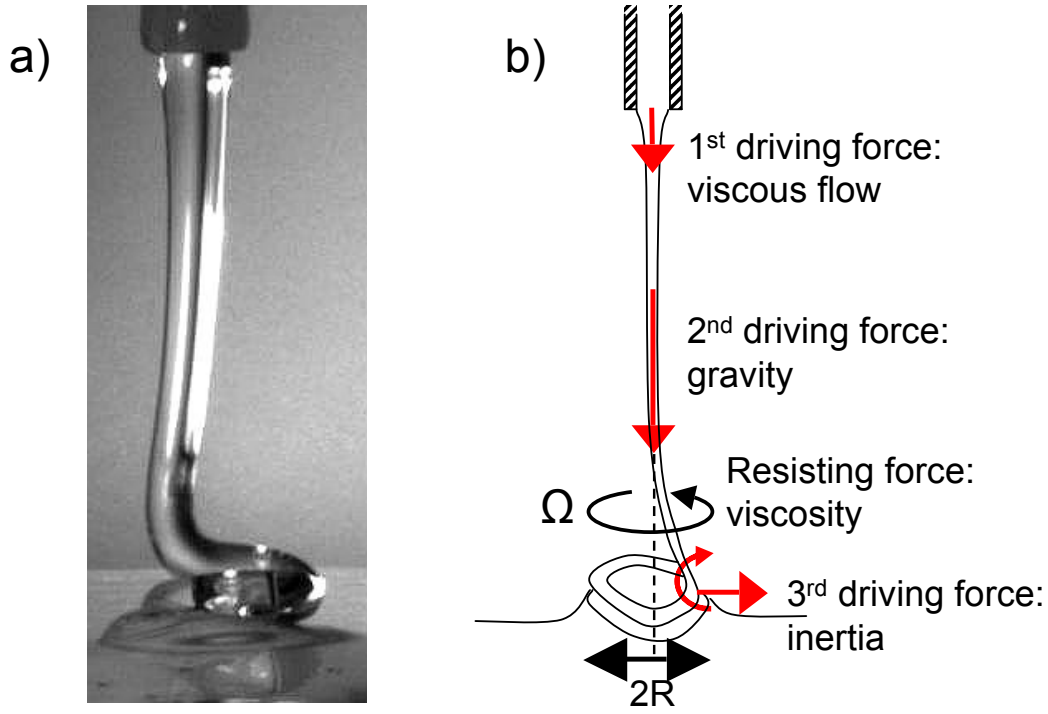
a)
b)
1st driving force:
viscous flow
2nd driving force:
gravity
Resisting force:
viscosity
Ω
3rd driving force:
inertia
2R

Fig. 2

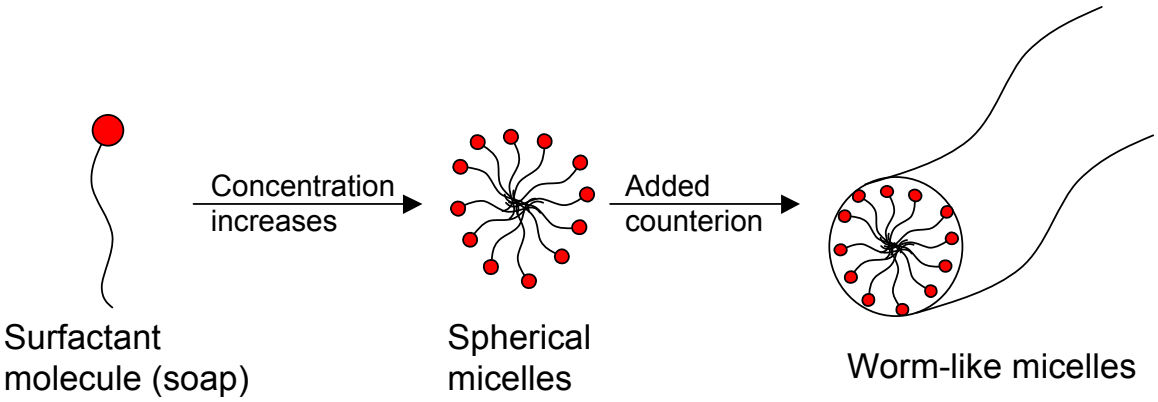
Concentration
increases
Added
counterion
Surfactant
molecule (soap)
Spherical
micelles
Worm-like micelles

Fig. 3

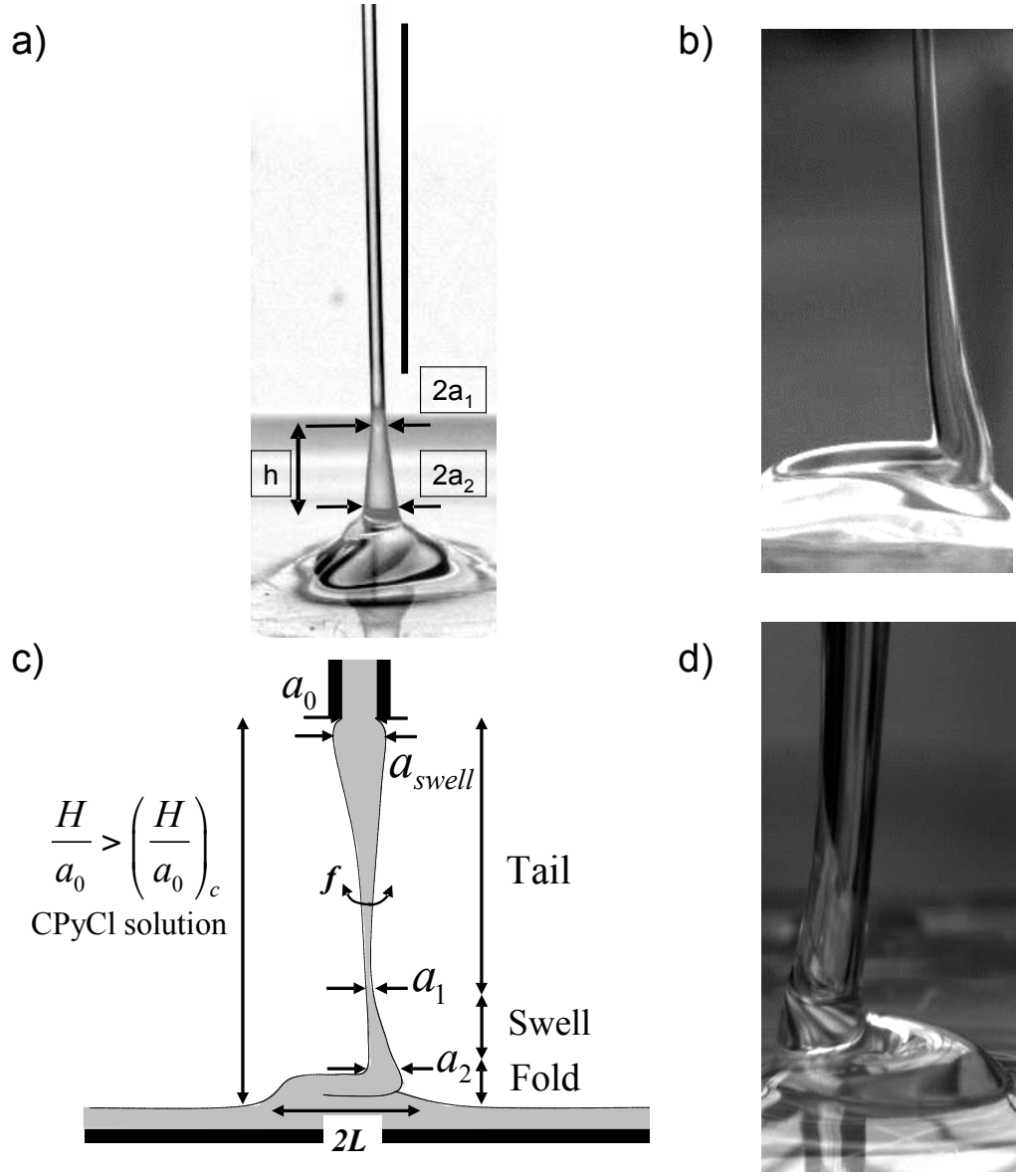
a)
b)
c)
d)
2a1
h
2a2
a0
aswell
H/a0 > (H/a0)c
CPyCl solution
f
Tail
a1
Swell
a2
Fold
2L

Fig. 4

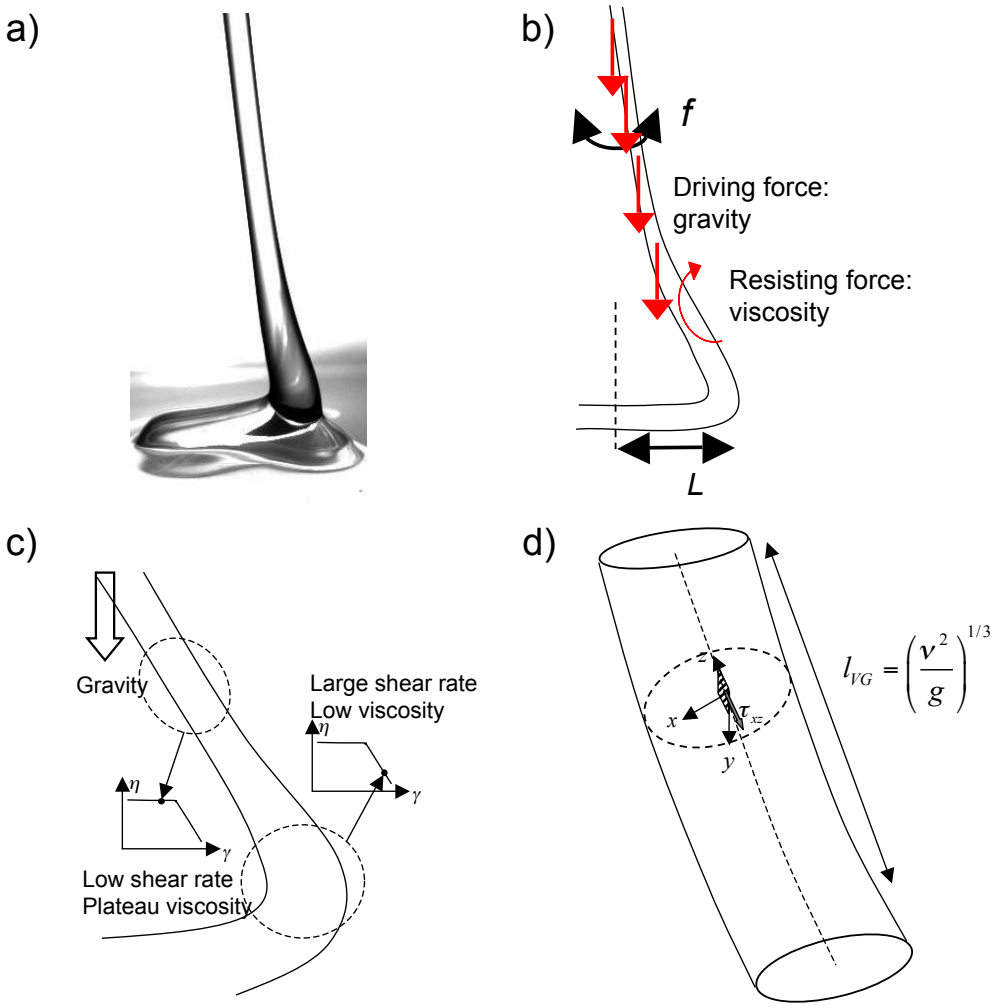
a)
b)
f
Driving force:
gravity
Resisting force:
viscosity
L
c)
Gravity
Large shear rate
Low viscosity
η
γ
η
γ
Low shear rate
Plateau viscosity
d)
z
x
y
τ_{xz}
$l_{VG} = \left(\frac{\nu^2}{g}\right)^{1/3}$

Fig. 5

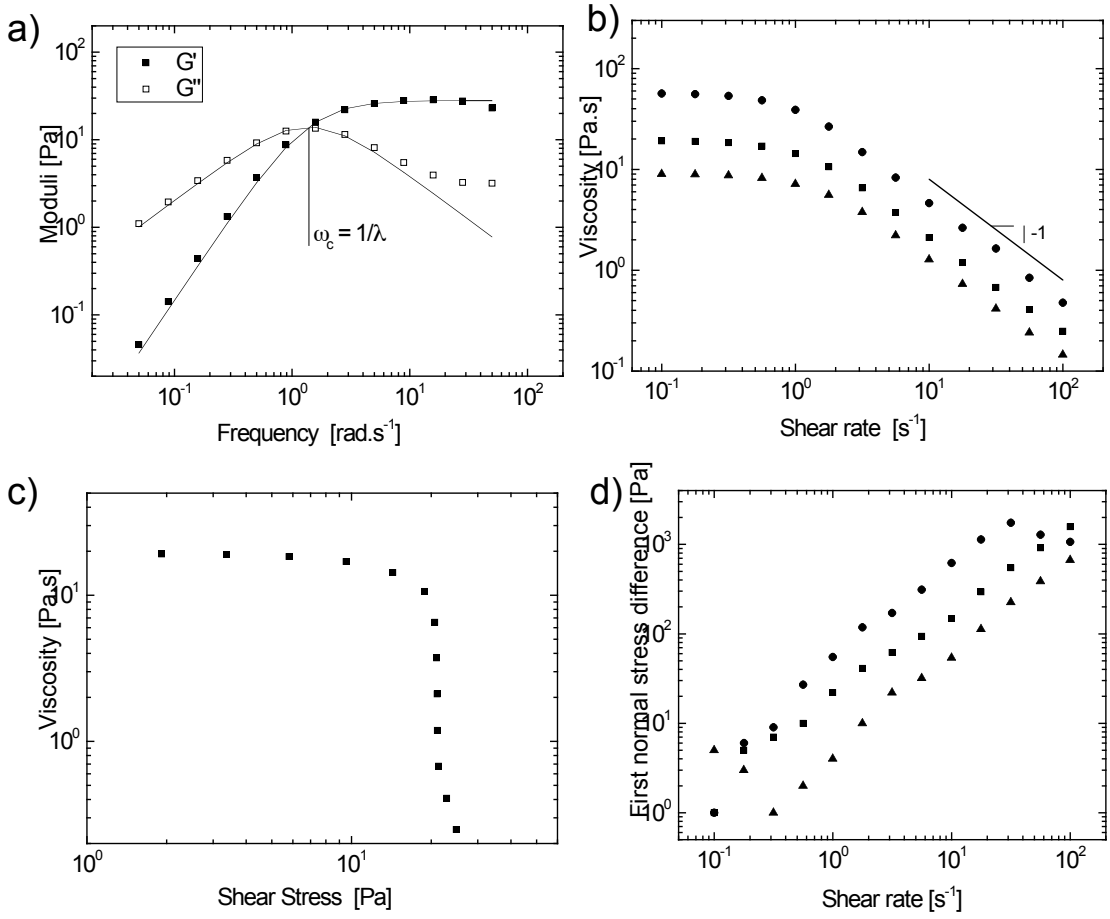
a)
G'
G''
Moduli [Pa]
$\omega_c = 1/\lambda$
Frequency [rad.s^{-1}]
b)
Viscosity [Pa.s]
-1
Shear rate [s^{-1}]
c)
Viscosity [Pa.s]
Shear Stress [Pa]
d)
First normal stress difference [Pa]
Shear rate [s^{-1}]

Fig. 6

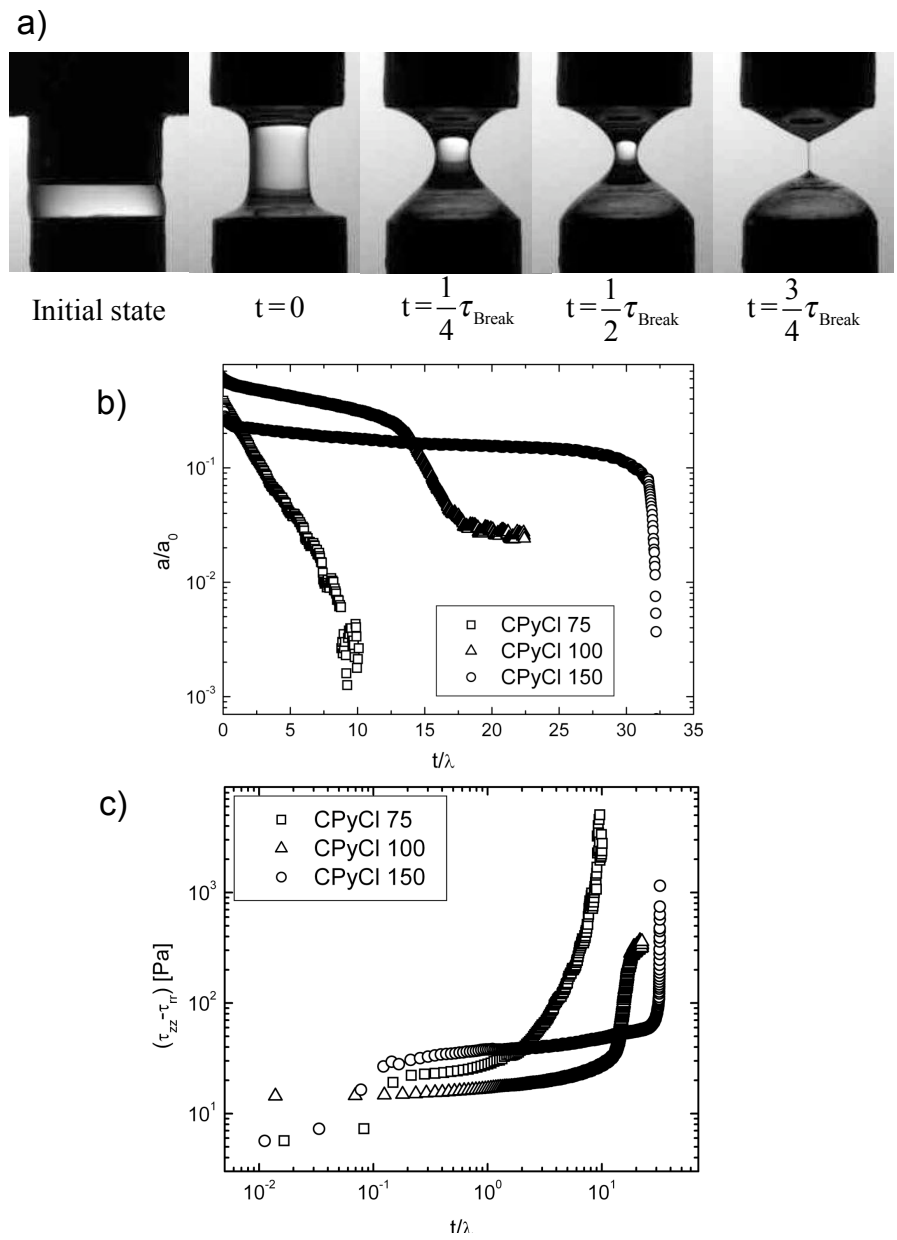
a)
Initial state
t = 0
t = 1/4 τ Break
t = 1/2 τ Break
t = 3/4 τ Break
b)
a/a0
t/λ
CPyCl 75
CPyCl 100
CPyCl 150
c)
(τzz - τrr) [Pa]
t/λ
CPyCl 75
CPyCl 100
CPyCl 150

Fig. 7

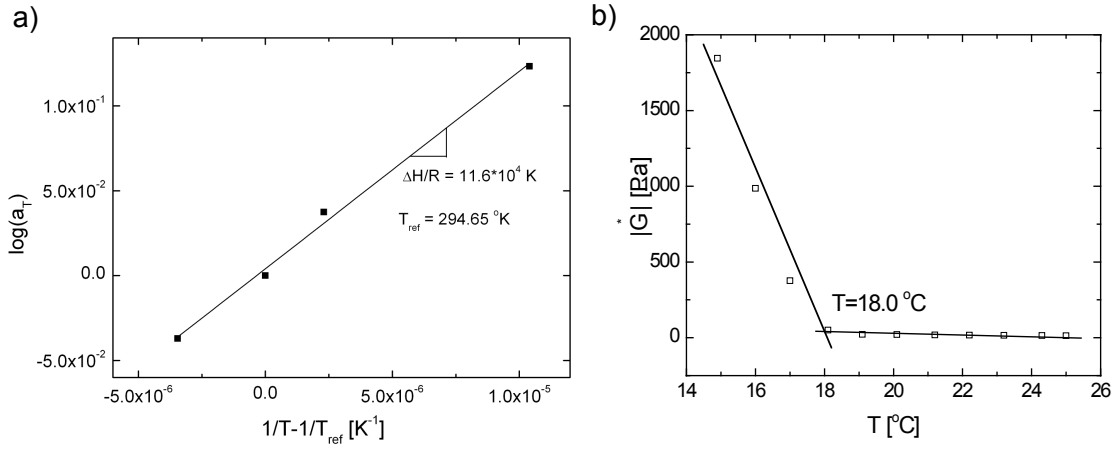
a)
1.0x10^-1
5.0x10^-2
0.0
-5.0x10^-2
log(a_T)
ΔH/R = 11.6*10^4 K
T_ref = 294.65 °K
-5.0x10^-6
0.0
5.0x10^-6
1.0x10^-5
1/T-1/T_ref [K^-1]
b)
2000
1500
1000
500
0
|G*| [Ra]
T=18.0 °C
14
16
18
20
22
24
26
T [°C]

Fig. 8

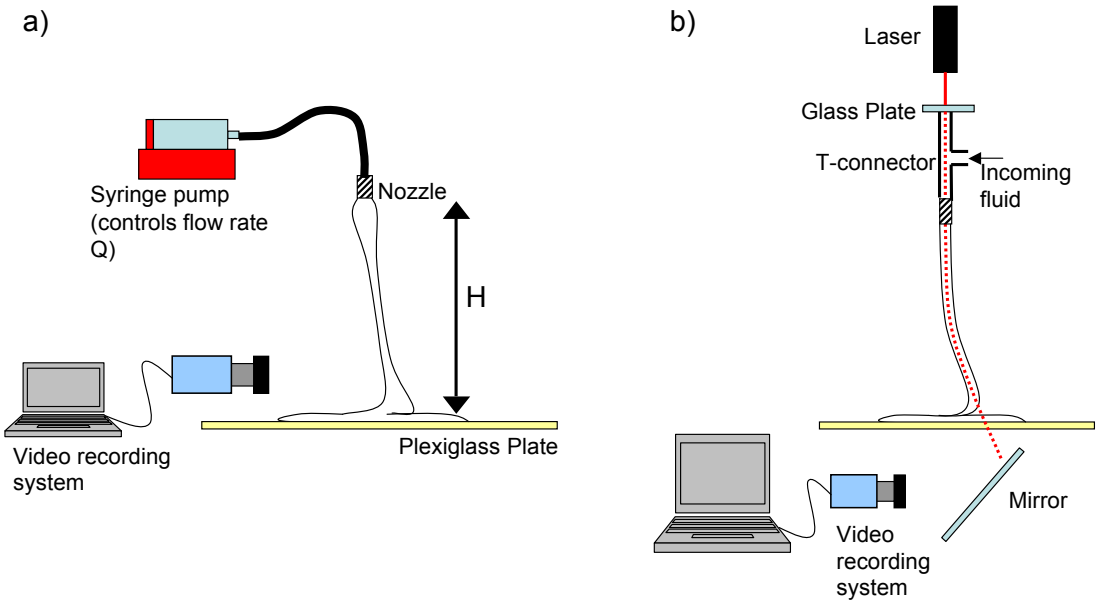
a)
Syringe pump
(controls flow rate
Q)
Nozzle
H
Video recording
system
Plexiglass Plate
b)
Laser
Glass Plate
T-connector
Incoming
fluid
Mirror
Video
recording
system

Fig. 9

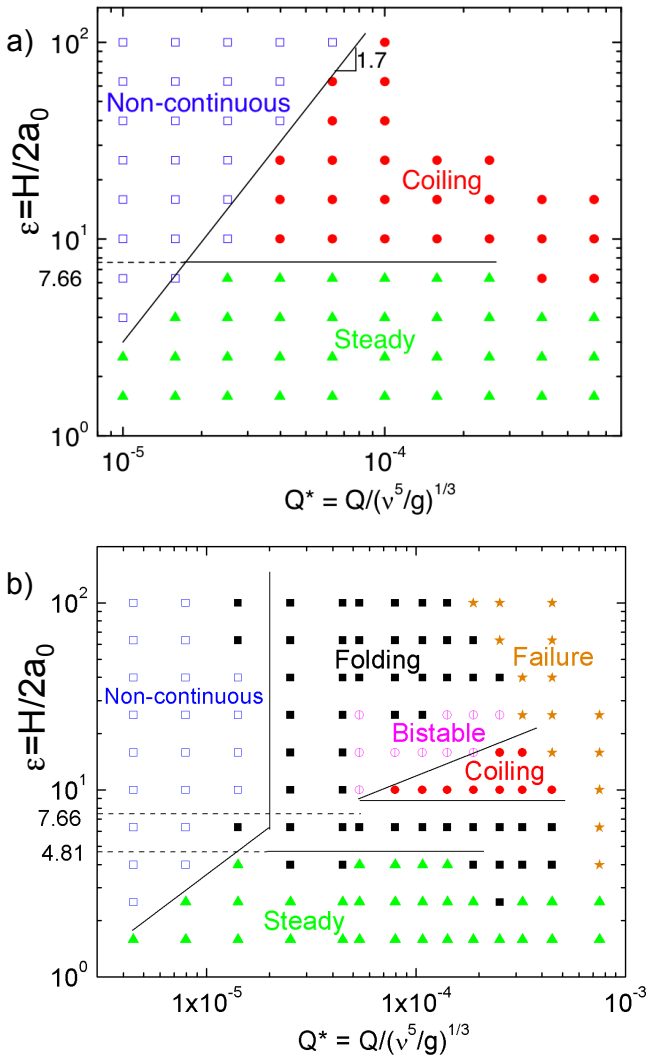
a)
Non-continuous
Coiling
Steady
1.7
7.66
ε=H/2a0
Q* = Q/(ν5/g)1/3
b)
Non-continuous
Folding
Failure
Bistable
Coiling
Steady
7.66
4.81
ε=H/2a0
Q* = Q/(ν5/g)1/3

Fig. 10

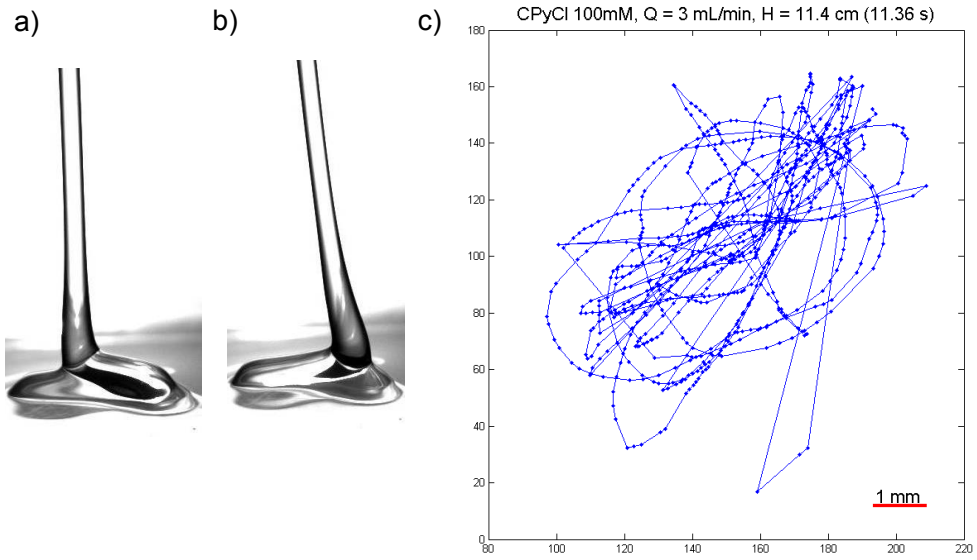
a)
b)
c)
CPyCl 100mM, Q = 3 mL/min, H = 11.4 cm (11.36 s)
1 mm
180
160
140
120
100
80
60
40
20
0
80
100
120
140
160
180
200
220

Fig. 11

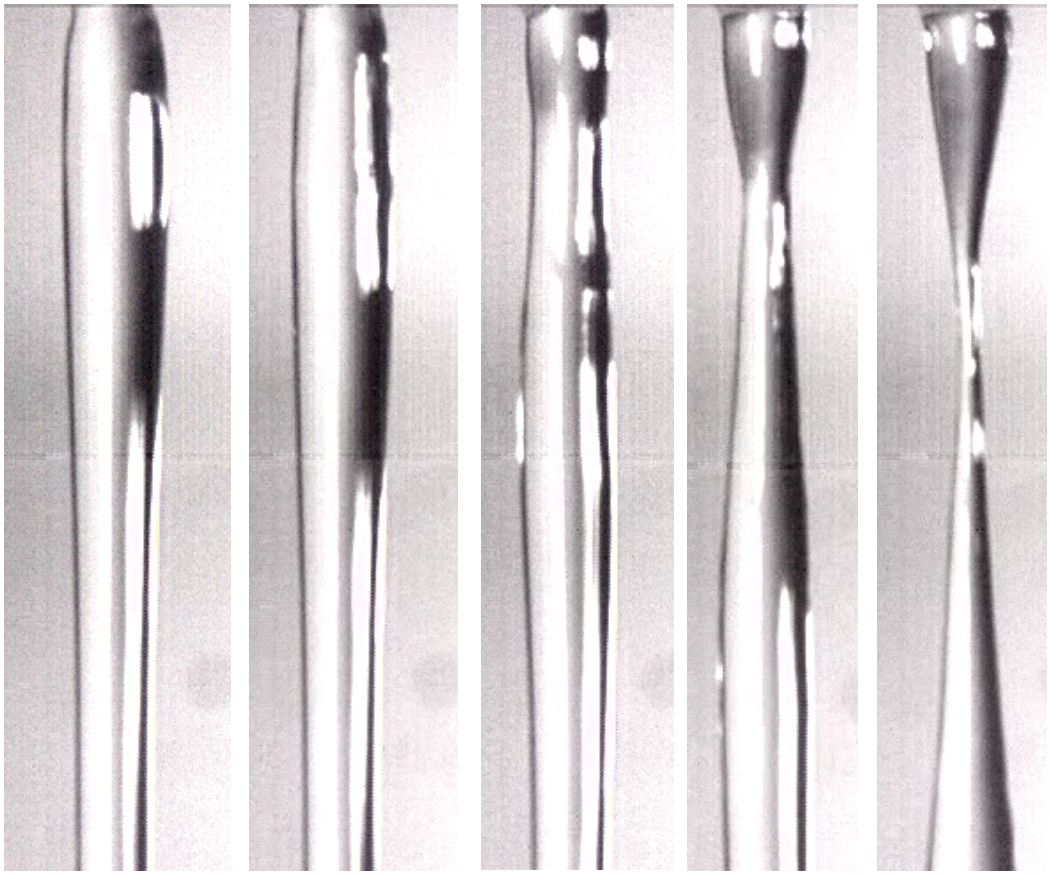

Fig. 12

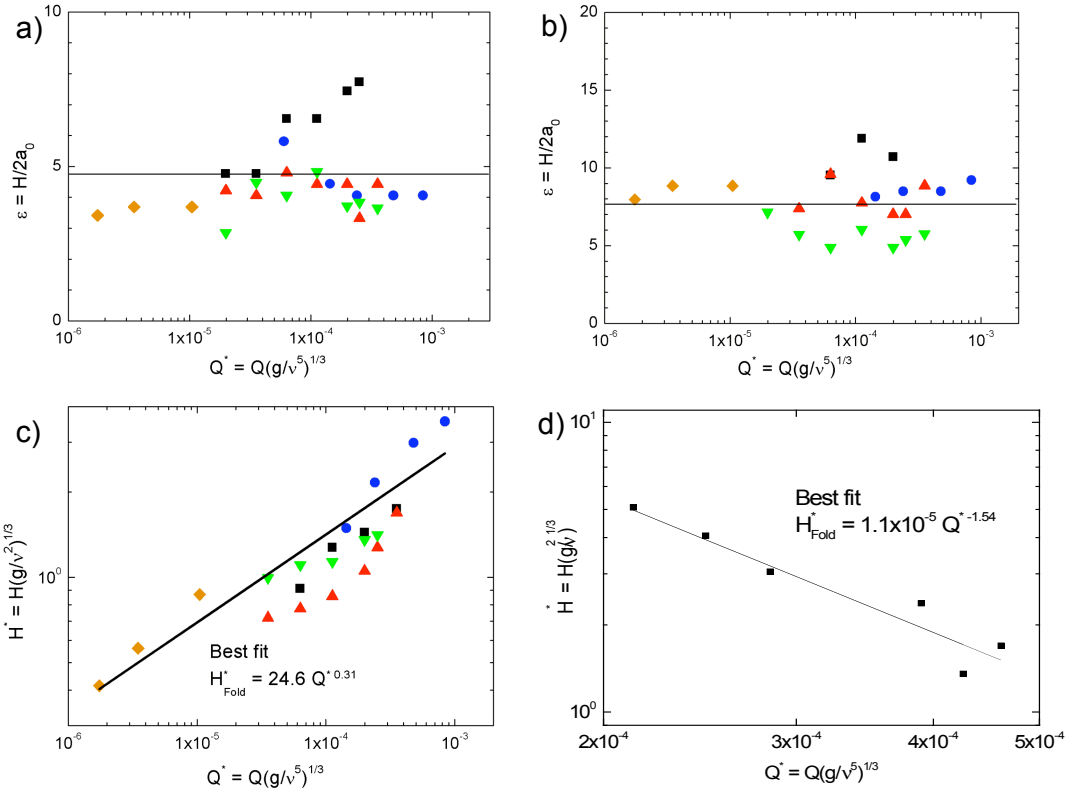
a)
b)
c)
d)
ε = H/2a0
Q* = Q(g/ν5)1/3
H* = H(g/ν2)1/3
Best fit
H*Fold = 24.6 Q*0.31
H*Fold = 1.1x10-5 Q*-1.54

Fig. 13

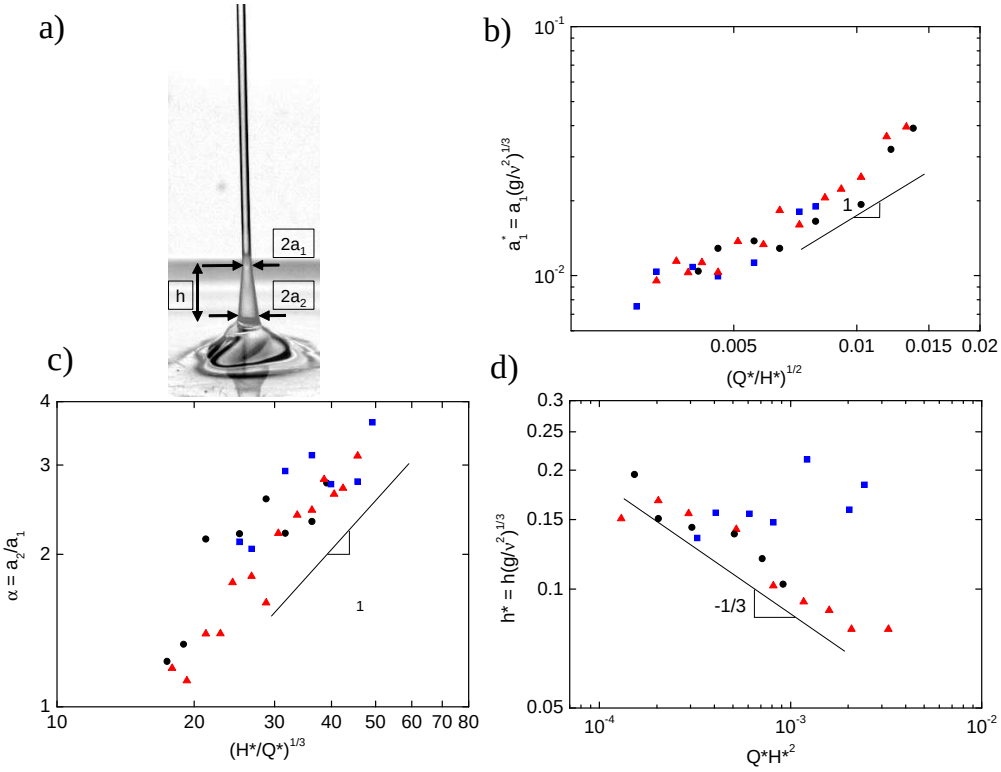
a)
b)
c)
d)
2a1
h
2a2
10-1
10-2
a1* = a1(g/ν2)1/3
1
0.005
0.01
0.015
0.02
(Q*/H*)1/2
α = a2/a1
4
3
2
1
10
20
30
40
50
60
70
80
(H*/Q*)1/3
0.3
0.25
0.2
0.15
0.1
0.05
h* = h(g/ν2)1/3
-1/3
10-4
10-3
10-2
Q*H*2

Fig. 14

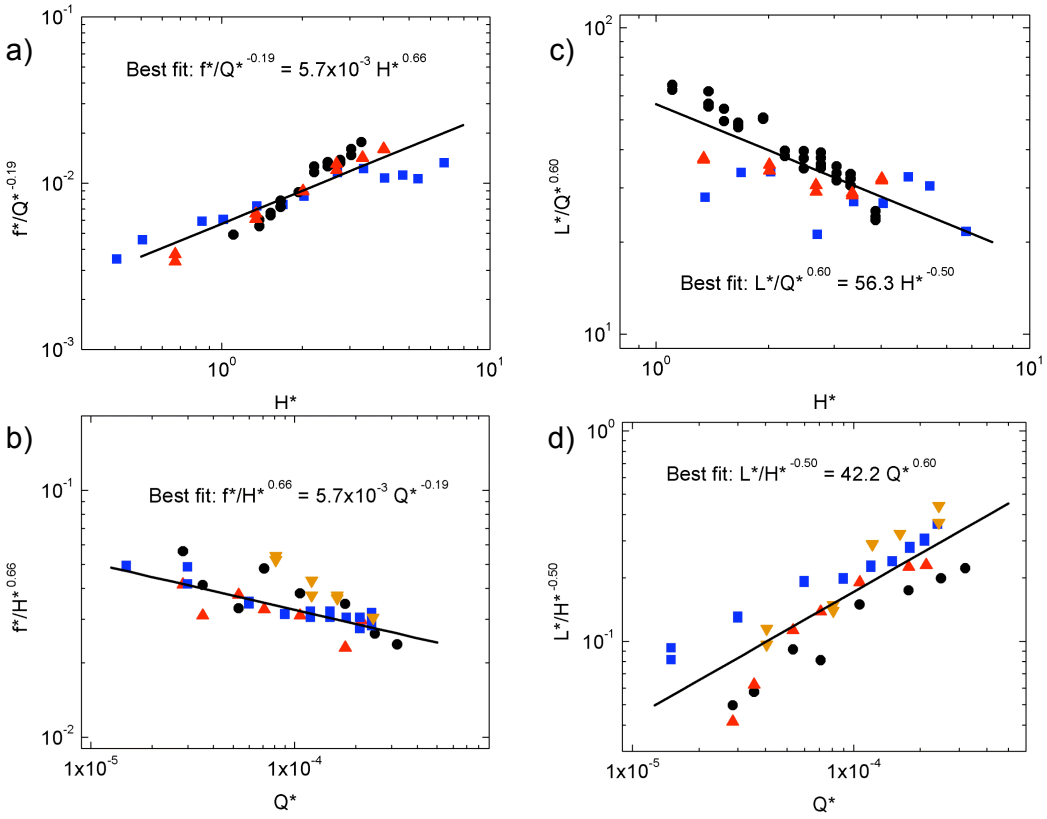
a)
Best fit: f*/Q* -0.19 = 5.7x10-3 H* 0.66
f*/Q* -0.19
H*
b)
Best fit: f*/H* 0.66 = 5.7x10-3 Q* -0.19
f*/H* 0.66
Q*
c)
Best fit: L*/Q* 0.60 = 56.3 H* -0.50
L*/Q* 0.60
H*
d)
Best fit: L*/H* -0.50 = 42.2 Q* 0.60
L*/H* -0.50
Q*

Fig. 15

Tables

Type of Motion	**Frequency**	**Radius/Amplitude**
Viscous Coiling	$H^{-1}Qa_0^{-2}$	H
Gravitational Coiling	$H^2Q^{-1/4}$	$Q^{1/4}$
Inertial Coiling	$H^{10/3}Q^{-1/3}$	$H^{-4/3}Q^{1/3}$
Viscous Folding	$H^{-2}Qa_0^{-1}$	H
Gravitational Folding	$H^{7/6}Q^{-1/6}a_0^{-2/3}$	$H^{-1/2}Q^{1/2}$
Inertial Folding	$H^{3/2}Q^{1/6}a_0^{-2/3}$	$H^{-2/3}Q^{1/3}$
Experiments Folding	$H^{0.66}Q^{-0.19}$	$H^{-0.50}Q^{0.60}$

Table 1: Theoretical scaling laws for the different flow regimes, with respect to the height of the fall, the flow rate and the radius, as well as the experimental results (the last row).

	CPyCl 75	**CPyCl 100**	**CPyCl 150**	**Silicone oil**
λ (s)	0.61	0.72	0.90	0
η_0 (Pa.s)	8.98	18.8	54.0	9.97
E_g	13.3	12.4	10.9	0

Table 2: Viscometric properties of the three CPyCl solutions studied in this work and the silicone oil at 22.5 ^{o}C.

	Overall exponent	**Range of exponents**
H^* dependence of f^*	0.66	$0.4 <-> 1.2$
Q^* dependence of f^*	-0.19	$-0.18 <-> -0.5$
H^* dependence of L^*	-0.50	$-0.1 <-> -0.7$
Q^* dependence of L^*	0.60	$0.45 <-> 0.8$

Table 3: Range of scaling exponents obtained for various series of experiments, compared to global scaling exponents obtained from regression of full data set.